Marine Structures 95 (2024) 103597

Contents lists available at ScienceDirect

Marine Structures

journal homepage: www.elsevier.com/locate/marstruc

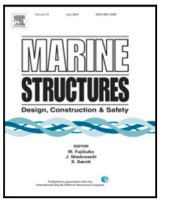

Research paper

Optimal control of wave cycloidal rotors with passively morphing foils: An analytical and numerical study☆

Abel Arredondo-Galeana [a,*], Andrei Ermakov [b], Weichao Shi [c], John V. Ringwood [b], Feargal Brennan [a]

[a] Department of Naval Architecture, Ocean and Marine Engineering, University of Strathclyde, 100 Montrose Street, Glasgow, G4 0LZ, UK
[b] Centre for Ocean Energy Research, Maynooth University, Maynooth, W23 A3HY, Co. Kildare, Ireland
[c] Mechanical Engineering and Marine Technology, School of Engineering, Newcastle University, Newcastle Upon Tyne, NE1 7RU, UK

ARTICLE INFO

Keywords:
Wave energy converter
LiftWEC
Cyclorotor
Fatigue analysis
Velocity control
Passive pitch

ABSTRACT

In this paper we perform an analytical and numerical study of the performance of a wave cycloidal rotor in irregular waves, with passively morphing foils and variable rotational velocity control. The performance is measured in two ways: Mechanical power, and fatigue damage in a sample stress hot spot located at the fixed end of the hydrofoils. We consider different strategies seeking to both maximise power extraction and reduce fatigue damage. To maximise power, we consider both constant and variable rotational speed. To mitigate fatigue damage, we consider, for the first time, morphing foils in the context of a wave cycloidal rotor. By testing these control strategies in isolation and in combination, and with the aid of high performance computations, we find that variable rotational speed, in combination with morphing foils, offers the best compromise to enhance power production with a reduced structural penalty on the sample stress hot spot. Hence, in this work, we demonstrate that novel control strategies, such as those proposed in this work, can hold the key in reducing the levelised cost of energy and accelerate the commercialisation of the next generation of lift-based wave energy converters.

1. Introduction

Wave cycloidal rotors are a novel type of wave energy converter (WEC) that have received an increased level of attention over the past decade. Recent efforts in the USA from Atargis [1] and other groups [2], the LiftWEC consortium in Europe [3], and academic efforts in China [4] are driving the momentum in the research of this type of WEC. Wave cycloidal rotors are a particularly enticing WEC due to their control versatility, submerged mode of operation and the potential for reduced levelised cost of energy [5,6]. Briefly, the device consists of a set of hydrofoils that rotate around a central shaft following the orbital motion of the wave particles, as shown in Figs. 1 and 2. The rotor operates near the water surface but remains submerged with interaction between the foils and waves generating lift forces on the foils, which then sustains the rotation of the device to generate electric power.

☆ This document is the result of the research project funded by the European Union's Horizon 2020 Research and Innovation Programme under Grant Agreement No 851885, and supported in part by a research grant from Science Foundation Ireland and the Sustainable Energy Authority of Ireland under SFI-IRC Pathway Programme 22/PATH-S/10793.

* Corresponding author.
E-mail addresses: abel.arredondo-galeana@strath.ac.uk (A. Arredondo-Galeana), andrei.ermakov@mu.ie (A. Ermakov), weichao.shi@newcastle.ac.uk (W. Shi), john.ringwood@mu.ie (J.V. Ringwood), feargal.brennan@strath.ac.uk (F. Brennan).

https://doi.org/10.1016/j.marstruc.2024.103597
Received 14 December 2022; Received in revised form 12 January 2024; Accepted 2 February 2024
Available online 6 February 2024

Nomenclature

a	Fourier series coefficient [–]
$\overline{a}$	intercept of vertical axis of SN curve [–]
A	wave amplitude [m]
b	Fourier series coefficient [–]
c	Fourier series coefficient [–]
C	hydrofoil chord length [m]
C_0	distance from pitching axis to quarter chord [m]
C_D	drag coefficient [–]
C_L	lift coefficient [–]
C_M	moment coefficient [–]
$C_{M,1/4}$	quarter chord moment coefficient [–]
C_P	distance from pitching edge to pitching axis [m]
d	Fourier series coefficient [–]
D	accumulated fatigue damage [–]
D_1	damage accumulated for rotation with the optimal constant velocity and rigid pitch [–]
D_2	damage accumulated for rotation with the optimal constant velocity and flexible pitch [–]
D_3	damage accumulated for rotation with the the optimal variable velocity and rigid pitch [–]
D_4	damage accumulated for rotation with the optimal variable velocity and flexible pitch [–]
D_w	Dawson function
$F(z,t)$	the complex potential for the point vortex [N]
F_L	lift force [N]
F_D	drag force [N]
F_T	tangential force [N]
F_R	radial force [N]
g	gravity constant [m^2/s]
h	total number of harmonics []
H	monochromatic wave height [m]
H_s	significant wave height [m]
I	Inertia of rotor [kg m^2]
I_{xx}	second moment of are of square hollow section [m^4]
J	mechanical power per second per span meter [W s^{-1} m^{-1}]
J_0	power generated for rotation with the wave frequency [W s^{-1} m^{-1}]
J_1	power generated for rotation with the optimal constant velocity and rigid pitch [W s^{-1} m^{-1}]
J_2	power generated for rotation with the optimal constant velocity and flexible pitch [W s^{-1} m^{-1}]
J_3	power generated for rotation with the optimal variable velocity and rigid pitch [W s^{-1} m^{-1}]
J_4	power generated for rotation with the optimal variable velocity and flexible pitch [W s^{-1} m^{-1}]
J_w	power available in irregular waves [W s^{-1} m^{-1}]
k	wave number [–]
m	mass of hydrofoil segment [kg]
$\overline{m}$	negative slope of the SN curve [–]
M_0	torsional moment [N m]
M	bending moment at stress hot spot of the foil [N m]
M_H	hydrodynamic moment [N m]
$\overline{M_H}$	mean hydrodynamic moment [N m]
M_P	torsional moment of spring [N m]

The use of lift forces, due to the wave hydrofoil interaction, contrasts with more traditional WECs, whose designs exploit buoyancy and/or diffraction forces [7–11]. At the same time, control technology is reaching a level of maturity for classical WECs [12,13], including experimental validation [14–16], while specific control strategies for wave cycloidal rotors are a topic of current research and development [17–19].

Cyclorotor-based WECs produce unidirectional rotation increasing the efficiency and reducing the cost of power extraction significantly in comparison with other WECs that typically require rectification of an oscillating motion [20–22]. In particular,

n_i	number of cycles in stress block i [–]
N_i	number of cycles to failure at stress range $\Delta\sigma$ [–]
P_i	the probability of the ith sea
R	radius of cyclorotor [m]
S	span of cyclorotors shaft [m]
$S_A(\omega_j)$	amplitude of the spectrum at the jth frequency
S_{PM}	Pierson–Moskowitz spectrum
SHS	square hollow section
t	time [s]
T	monochromatic wave period [s]
T_0	the time interval for power calculation [s]
T_e	panchromatic wave energy period [s]
T_{ext}	time interval for energy calculation [s]
T_p	panchromatic wave peak period [s]
$\mathbf{u}$	rotational velocity of the foil [m/s]
$\mathbf{U}$	relative foil/fluid velocity [m/s]
$\overline{\mathbf{U}}$	mean inflow velocity [m/s]
$\mathbf{w}$	wave induced fluid velocity [m/s]
$\mathbf{w}_{\mathbf{\Gamma}}$	foil induced fluid velocity [m/s]
x	stream-wise coordinate in the z-plane [m]
y	normal coordinate from the mean water level [m]
y_0	submergence of rotor [m]
y_{xx}	distance from symmetric horizontal axis to outer shell of the square hollow section [m]
z	complex coordinate
α	angle of attack [°]
$\overline{\alpha}$	non-zero mean angle of attack [°]
β	inflow angle of U [°]
γ	JONSWAP spectrum factor [–]
Γ	instantaneous circulation of point vortex [m^2/s]
ζ	position of point vortex in the z-plane
ζ'	position of the mirror point vortex in the z-plane
η	wave phase
θ	azimuthal position of rotor [°]
$\dot{\theta}$	rotational frequency or rate of rotor [°/s]
$\dot{\theta}_0$	optimal rotational frequency or rate of rotor [°/s]
$\ddot{\theta}$	rotational acceleration of rotor [°/s^2]
κ	spring stiffness [N/m]
λ	proportionality coefficient between wave peak and energy periods [–]
ρ	fluid density [kg/m^3]
σ	parameter of JONSWAP spectrum [–]
$\overline{\sigma}$	structural stress [MPa]
τ	time parameter [s]
$\mathcal{T}_{PTO}$	power take-off torque [N m]
$\mathcal{T}_{Wave}$	hydrodynamic torque [N m]
ϕ	torsional spring deformation or pitch angle displacement [°]
ψ	the initial angular position of each hydrofoil [°]
ω	wave frequency [°/s]
ω_p	peak wave frequency [°/s]

given that the naturally induced motion is rotational, issues such as the finite stroke displacement of linear generators do not arise. Furthermore, most traditional WECs are designed to work primarily at one, or at a limited range of, wave velocities and frequencies with maximum efficiency. In contrast, the reconfigurable abilities of the hydrofoils of a wave cycloidal rotor can significantly expand the range of useful excitation. For example, pitch control of the hydrofoils can modulate wave loading on the device, particularly

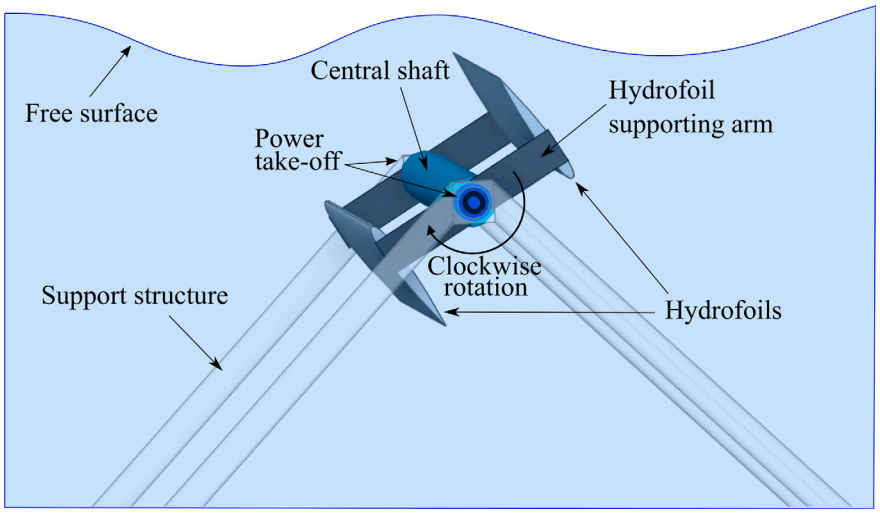

Fig. 1. Schematic of a wave cycloidal rotor operating clockwise under the free surface. The main structural components are: The hydrofoils, central shaft, supporting arms and power take-off (PTO) units.

during high power or extreme wave conditions. Another possibility is variable rotational velocity, which has been demonstrated to be a promising technology for cyclorotors to enhance power extraction in regular and irregular waves [17,18] .

However, despite the aforementioned operational advantages, the hydrodynamic and structural complexity of cyclorotors also makes them vulnerable to fatigue damage and operational breakdown. In fact, power enhancement strategies, such as variable rotational speed, may have structurally undesirable side effects, since larger loads could cause mechanical failure and may cause irreparable damage. Therefore, load alleviation interventions could be key and complementary to the optimal operation of wave cycloidal rotors. An example of such technologies are foils that morph due to fluid forces.

Morphing foils, modelled as passive pitch mechanisms, have shown to reduce loading in cross flow [23–26] and tidal turbines [24,27,28], when subject to unsteady flow. It can then be expected that load alleviation is also attainable in wave cycloidal rotors equipped with morphing foils. This is due to the similarly unsteady nature of the flow surrounding wave cycloidal rotors [29,30]. Nonetheless, a study on the effect of morphing foils has not yet been available in the cyclorotor literature. Hence, the structural impact of variable rotational speed, and the role of morphing foils, in wave cycloidal rotors that operate in irregular waves are the research gaps addressed in this paper.

We postulate the hypothesis that, by combining rotational velocity control and passive morphing of the hydrofoils, we can enhance power extraction while, at the same time, reduce the structural penalty on the stress hot spots of the hydrofoils. We investigate our hypothesis through four control cases: (1) constant rotational velocity and rigid foil, (2) constant rotational velocity and passively morphing foil, (3) variable rotational velocity and rigid foil, and (4) variable rotational velocity and passively morphing foil.

The article is organised as follows: In Section 2, we present an introduction to the operation of wave cycloidal rotors, followed by the concepts of a passively pitching foil in irregular waves and the fatigue damage computation at the stress hot spot of the foils. In Section 3, we introduce the hydrodynamic model, which accounts for irregular sea states, to reflect realistic sea behaviour. Subsequently, in Section 4, we discuss the control strategy to combine variable rotational speed with morphing foils. In Section 5, power and fatigue damage results are discussed for the four sample control cases. Lastly, in Section 6, we present our conclusions.

2. Operational principle and structural model

2.1. Mechanical model of the rotor

The concept of a wave cycloidal rotor is depicted in Fig. 1. The figure shows a two foil rotor with symmetric NACA 0015 hydrofoils, as initially proposed within the LiftWEC project [31], operating under the free surface. In this example, the rotor is supported by two tubular triangular frames that are anchored to the sea bed. The support structure is shown as transparent to highlight the main rotor components. The rotor is composed of the hydrofoils, central shaft, supporting arms and power take-off (PTO) units. The PTO units are motors with a stator and rotating part. The stator is held by the support structure and the rotating part is attached to the central shaft through bearings.

The operation principle of the rotor is summarised in Fig. 2. The figure shows a side view of the rotor. The origin of the reference frame $O(x, y)$ is located above the central shaft and at the mean sea level. The rotor has a submergence y_0 measured from the mean sea level to the central shaft. The radius of the rotor is denoted by R. The wave propagates from left to right and the wave particle

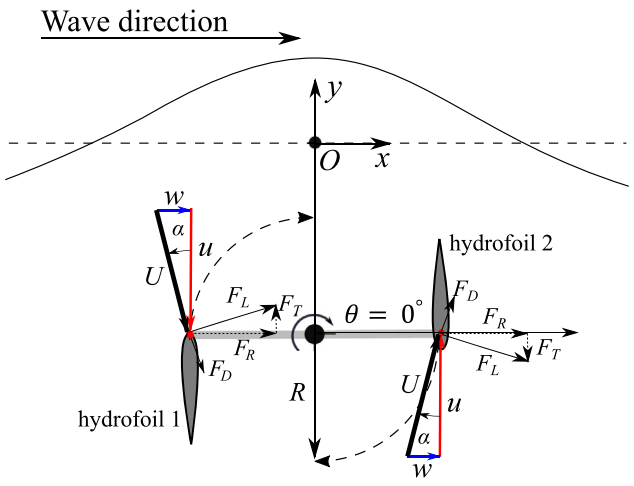

Fig. 2. Side view of a wave cycloidal rotor, showing the lift and drag forces (F_L, F_D) on the hydrofoils, the radial and tangential force components (F_R, F_T), the wave velocity w, the velocity due to the rotation of the hydrofoils u, and the relative fluid velocity to the foil U. The origin O of the reference frame is defined at the mean sea level above the central shaft.

motion is clockwise [32]. The rotation of the hydrofoils follows the circular wave particle motion generating lift F_L and drag forces F_D, such that

$$F_L = \frac{1}{2}\rho C S C_L(\alpha)|U|^2 \tag{1}$$

and

$$F_D = \frac{1}{2}\rho C S C_D(\alpha)|U|^2, \tag{2}$$

where ρ is the fluid density, U is the relative fluid velocity to the foil, S is the span of the hydrofoil, C is the chord length, and $C_L(\alpha)$ and $C_D(\alpha)$ are the lift and drag force coefficients, which are both a function of the angle of attack α. We note that U is composed of the vectorial sum of the wave velocity w and the velocity component due to the rotation of the foil u, and that α is measured between u and U, as illustrated in Fig. 2. The figure also shows the radial F_R and tangential forces F_T acting on the hydrofoils, which are the normal and tangential projections of F_L and F_D along the chord of the hydrofoil.

2.2. Morphing foil model

Morphing foils, modelled as passively pitching systems, have shown to be a promising technology for peak loading alleviation in tidal turbines [24,27,28,33]. However, to date, passive compliance has not been studied for wave energy devices and, in particular, for wave energy cyclorotors operating in irregular sea states. In this article, we develop a novel model for passive morphing of a foil in wave cycloidal rotors, based on the work performed for tidal turbines by Pisetta et al. [28]. We refer to their model as the single spring model and present first a brief summary as follows.

The single spring model represents a morphing foil by simulating compliance through a torsional spring attached to the pitching axis of the foil [28]. The initial equilibrium position is shown in Fig. 3a. The pitching axis is located near the leading edge of the foil and the distance from the pitching axis to the quarter chord is denoted as C_0. The torsional spring, which is located at the pitching axis, is pretensioned and its torsional moment (M_0) opposes and balances the mean hydrodynamic moment of the foil ($\overline{M_H}$). Because M_0 and $\overline{M_H}$ are opposite and equal to each other, a nonzero mean angle of attack $\overline{\alpha}$ can be sustained in the foil, as depicted in Fig. 3a. In Fig. 3a, the mean inflow velocity is $\overline{U}$.

Subsequently, during operation, the foil pitches around its pitching axis in the presence of periodic inflow oscillations and around $\overline{\alpha}$. This scenario is illustrated in Fig. 3b. Even though the foil pitches, the spring moment M_0 is considered constant because the spring is of very low stiffness. The change in the inflow is $\delta\alpha$, the change in M_H is δM_H, and the change in F_R is δF_R. Because the pitching axis is upstream of the quarter chord of the foil, the pitching motion opposes $\delta\alpha$. Hence, the angle of attack on the foil α and peak loading are attenuated. Because $\overline{\alpha}$ is maintained, mean power production remains unaltered. We note that, in Fig. 3b, U is the new inflow velocity acting on the foil, ϕ is the pitching angle of the foil and α is the new angle of attack on the foil after the pitching motion.

In a wave cycloidal rotor, the single spring model could work for regular sea state operation. This is because the angle of attack of the foil oscillates around a nonzero mean angle of attack [34]. However, for an irregular sea state, the mean angle of attack on the hydrofoils is zero. Therefore, the mean hydrodynamic moment is also zero and the moment provided by a single pretensioned spring cannot be balanced. In Fig. 4, we illustrate, as an example, the time series of α for one of the hydrofoils of the cyclorotor in

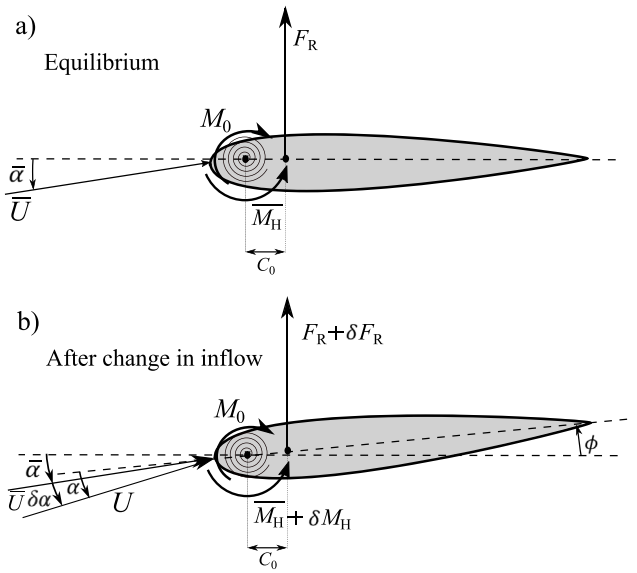

Fig. 3. Single spring model from Pisetta et al. [28] showing (a) the equilibrium position of the morphing foil, modelled with the single spring model with a non zero mean angle of attack $\bar{\alpha}$ and a mean inflow $\bar{U}$, and (b) the new equilibrium position after a change in the inflow and after the foil pitches by an angle ϕ.

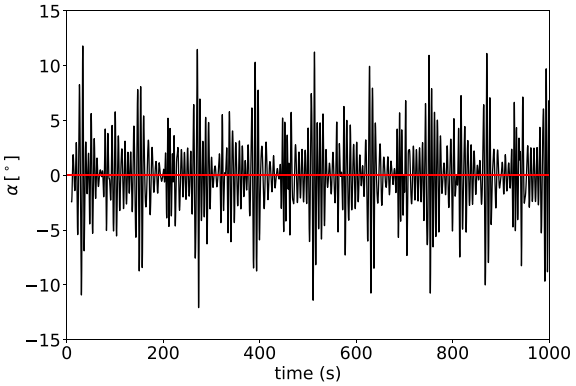

Fig. 4. Angle of attack oscillations in one of the foils in an irregular sea state ($T_P = 6$ s, $H_S = 1$ m). The horizontal red line shows the mean angle of attack.

an irregular sea state ($T_p = 6$ s and $H_s = 1$ m). The time series shows that the mean angle of attack in the hydrofoil of the cyclorotor is 0°. Note that the computation of α is performed with the hydrodynamic model, which is introduced later in Section 3.

Secondly, in the single spring model, developed for tidal turbines, the hydrodynamic moment coefficient is linearised, due to the assumption of small changes in the angle of attack. This assumption does not apply to the case of a cyclorotor foil in panchromatic waves [17]. As a result, the hydrodynamic moment coefficient cannot be linearised but, instead, its exact value needs to be computed.

Lastly, the assumption of a very low stiffness spring would yield a hydrofoil that is very sensitive to inflow changes and therefore, in a cyclorotor subject to irregular waves, the system could become unstable. As such, we consider a stiffness that will allow the foil to pitch, but that still poses some resistance to deformation. This could represent, for example, the deformation of a flap near the trailing edge of a foil [24].

Therefore, here, we develop a model to represent a passively morphing foil that pitches in the context of a cyclorotor. The model compensates for the lack of a nonzero mean hydrodynamic moment by the addition of a second torsional spring at the pitching axis. We refer to the model as the dual spring model. The equilibrium position of the foil of the cyclorotor is depicted in Fig. 5. The foil is at rest and free to pitch around the pitching axis. The pitching axis is located at a distance $C_p = 0.1C$ from the leading edge. The equilibrium position is enforced with two pretensioned springs that oppose each other around the pitching axis. The moments are denoted as $M_{0,1}$ and $M_{0,2}$. Because both moments are greater than the weight of the foil and than the buoyancy force, the foil remains at a zero angle of attack in equilibrium.

When the rotor spins in the presence of waves, an instantaneous change in the hydrodynamic moment δM_H will occur due to a change in the inflow angle of attack and a new equilibrium position is reached. We depict this scenario in Fig. 6. In Fig. 6, the change

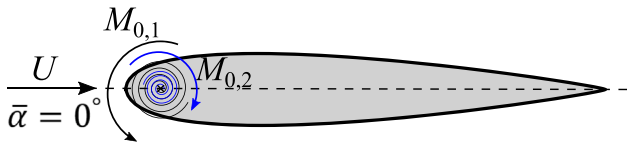

Fig. 5. The equilibrium position of a morphing foil modelled with the dual spring model for a wave cycloidal rotor operating in irregular waves, where the mean angle of attack is $\alpha = 0°$.

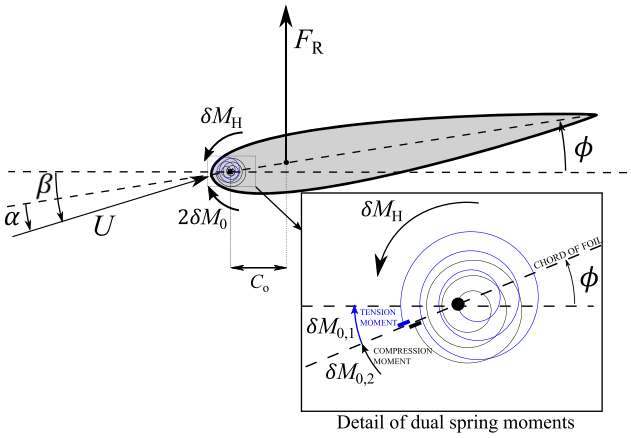

Fig. 6. (a) The new equilibrium position of the morphing foil modelled with the dual spring model after a small change in inflow angle. The inset of the figure shows the dual spring system.

in the inflow angle is defined as β, and is measured from the line tangent to the circumferential path of the rotor to the direction of the inflow angle U. Subsequently, because of the change in the direction of U, δM_H pitches the foil up and a displacement from the neutral position occurs. Because the springs are of low stiffness, but rigid enough to oppose a resistance to the pitching motion, the displacement from the neutral position causes a change in the torsional moment of each spring δM_0. We show the torsional moments of each spring $\delta M_{0,1}$ and $\delta M_{0,2}$ due to tension and compression, respectively, in the inset of Fig. 6. Both of these moments oppose δM_H. As such, the new equilibrium position will be achieved when

$$2\delta M_0 = \delta M_H. \tag{3}$$

In Eq. (3)

$$\delta M_0 = \kappa\, \phi, \tag{4}$$

where κ is the stiffness of the spring and ϕ is the pitching angle of the foil. In Eq. (3), the change in the hydrodynamic moment δM_H is defined as

$$\delta M_H = \frac{1}{2}\rho\, C_M\, C^2\, S\, |U|^2, \tag{5}$$

where C_M is the hydrodynamic pitching moment coefficient, ρ is the density of the fluid, U is the relative fluid velocity, S is the span of the foil and C is the chord length. In Eq. (5), C_M is obtained by translating the quarter chord hydrodynamic pitching moment $C_{M,\frac{1}{4}}$ to the pitching axis of the hydrofoil, such that

$$C_M = C_{M,\frac{1}{4}}(\alpha) + C_0\,[C_L(\alpha)\cos(\alpha) + C_D(\alpha)\sin(\alpha)], \tag{6}$$

where C_0 is the distance from the quarter chord position to the pitching axis. We note that the pitching axis is located at a distance of $C_p = 0.1C$ from the leading edge; therefore, $C_0 = 0.15C$. We recall that, for symmetric foils, such as those used in this cyclorotor, $C_{M,\frac{1}{4}}(\alpha) = 0$ [35].

Substituting relations (4), (5) and (6) into the moment balance given by Eq. (3), we obtain a nonlinear equation which is solved for ϕ, such that

$$\kappa\phi = \frac{1}{4}\rho\,(C_0\,[C_L(\alpha)\cos(\alpha) + C_D(\alpha)\sin(\alpha)])\,C^2\,S\,|U|^2 \tag{7}$$

where

$$\alpha = \beta - \phi. \tag{8}$$

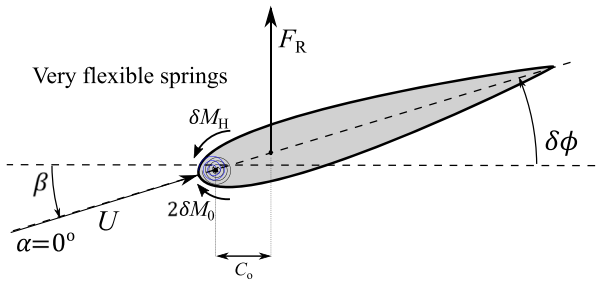

Fig. 7. The new equilibrium position of the morphing foil modelled with the dual spring model with very flexible springs.

In Eq. (8), β is the angle between the tangent to the circular trajectory of the foil and the relative fluid velocity U, as indicated in Fig. 6. For a rigid foil that does not pitch, $\beta = \alpha$. In contrast, when the foil pitches by ϕ, Fig. 6 shows that α, which is measured between the chord line and U, decreases. Therefore, the radial force F_R on the foil should also decrease.

Although a well tuned dual spring model reduces α and the change in the hydrofoil loading, a very low stiffness could come at a price. If the stiffness is too low, then $\beta = \phi$ and, therefore, $\alpha = 0°$. We depict this scenario in Fig. 7. As such, the ideal stiffness of the springs is one that reduces α, but does not nullify it. Hence, a spring system of intermediate stiffness could represents the behaviour of a realistic morphing structure where the deformation is concentrated towards the trailing edge of the hydrofoil.

2.3. Fatigue damage assessment

The methodology to compute the fatigue damage on the sample stress hot spot of the cyclorotor is presented in this section. The fatigue damage on a stress hot spot due to an ith sea state can be determined through Miner's rule [36,37], such that

$$D_i = \sum_{j=1}^{b} \frac{365 \times 24 \times P_i}{t} \frac{n_j}{N_j} \frac{1}{S}. \tag{9}$$

In Eq. (9), we define D_i as the accumulated fatigue damage per span metre for the ith sea state, P_i is the probability of occurrence of the ith sea state, t is the duration of the stresses time series in the hot spot, n_j is the number of cycles at stress range $\Delta\overline{\sigma}_j$, N_j is the number of cycles to failure at stress range $\Delta\overline{\sigma}_j$, b is the total number of stress blocks, and S is the span of the foil.

In Eq. (9), the probability P_i of the ith sea state is obtained from the wave climate from the HOMERE database from Ifremer [38]. The data is shown in Fig. 8 and corresponds to a point located at 47.84° N, 4.83° W on the North Atlantic coast of France. Each sea state in the database has a duration of 1 h and the data extends for a period between 2001 and 2010. Note that the database provides the energy period T_e, rather than the peak period T_p. For our hydrodynamic model, the conversion between T_e and T_p is performed through $T_e = \lambda T_p$ [39] . Hence, by considering a JONSWAP spectrum of shape factor 3.3, $\lambda = 0.9$ [40].

Since the data presented in Fig. 8 contains 120 sea states and 78,879 events, equivalent to 9 years of sea data, to perform our damage computations, we downsampled the grid from 120 sea states to 30 sea states over the range of 6 s $\leq T_p \leq$ 16 s and 1 m $\leq H_S \leq$ to 5 m, in steps of 2 s and 1 m, respectively. This window of sea states accounts for a total probability of occurrence of 98%. As such, the P_i values of Fig. 8 are grouped in representative clusters around a reduced grid of 30 sea states. Subsequently, the computed values of damage are interpolated to a finer grid of $21T_p$ and $25H_s$ to present our results. The same interpolation procedure is applied to present the mechanical power results computed with the control strategy presented in Section 4.

In Eq. (9), the number of cycles to failure N, for any given jth stress range, is obtained from the SN curve of the specific material. The SN curve gives the relationship between the stress range $\Delta\overline{\sigma}$ and N, and is given by

$$\log N = \log \overline{a} - \overline{m} \log \Delta\overline{\sigma}, \tag{10}$$

where N is the number of cycles to failure at stress range $\Delta\overline{\sigma}$, $\overline{m}$ is the negative inverse slope of the SN curve and $\log \overline{a}$ is the intercept of the $\log N$ axis by the SN curve. In this work, we use an SN curve of type C for offshore steel in seawater with cathodic protection [36]. This type of curve is recommended for smooth extruded finishes, such as that of the hydrofoils in a cyclorotor. We plot the corresponding SN curve in Fig. 9.

Eq. (10) can be rewritten in exponential form, such that

$$N = \overline{a} \Delta\overline{\sigma}^{-\overline{m}}, \tag{11}$$

where $\overline{a}$ and $\overline{m}$ are properties of the material. We utilise this expression to compute N for the jth stress range in Eq. (9).

In this paper, $\Delta\overline{\sigma}$, which refers to the stress range measured from peak to trough and vice-versa, is obtained from the time series of the bending stresses $\overline{\sigma}$ measured at one of the fixed ends of the hydrofoils. The number of cycles n of each $\Delta\overline{\sigma}$ was computed through a Rainflow cycle counting algorithm, as recommended by the ASTM E–1049 Standard Practices for Cycle Counting in Fatigue Analysis [41]. The stress hot spots are illustrated in Fig. 10. Because the foil is symmetric in the spanwise direction and because we assume two dimensional flow, i.e. large span foils, we consider $\Delta\overline{\sigma}$ at both hot spots to be equal, and therefore we compute the fatigue damage in one hot spot only.

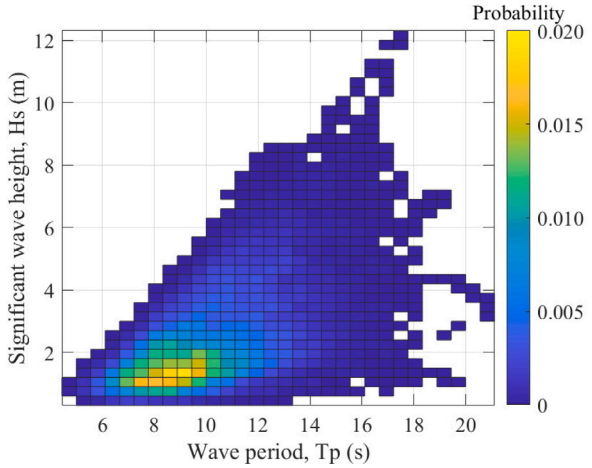

Fig. 8. Probability data of HOMERE database for a point in the North Atlantic coast of France with T_p and H_s in the horizontal and vertical axis, respectively.

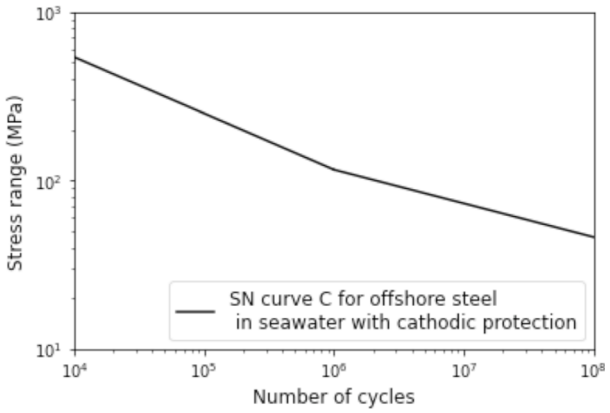

Fig. 9. SN curve of type C for offshore steel in seawater with cathodic protection.

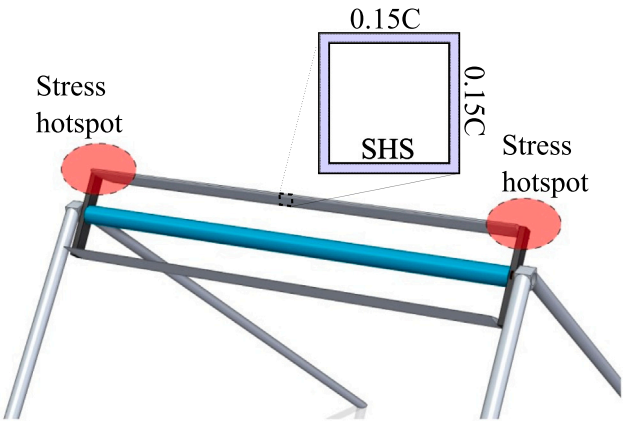

Fig. 10. Stress hot spots at fixed end of foils in wave cycloidal rotor.

The stresses on the hotspots are computed following the procedure described in [29,34,42]. As part of the procedure, we approximate the cross section of the foil as a square hollow section (SHS) of dimension 0.15C × 0.15C and a skin thickness of 10 mm. The cross section is shown in the inset of Fig. 10. The second moment of area I_{xx} of the cross section depends mainly on the height. As such, the SHS approximation provides a baseline for mechanical design and for the first pass of our fatigue damage analysis. Furthermore, as part of the procedure to compute the bending stresses, the bending moments are computed from the radial forces acting on the foil by assuming that the foil is a fixed beam subject to a uniformly distributed loading. Hence, $\overline{\sigma}$ at just one of the foil stress hot spots is computed, such that

$$\overline{\sigma} = \frac{M y_{xx}}{I_{xx}}, \tag{12}$$

where M is the bending moment at the stress hot spot, y_{xx} is the distance from the symmetric horizontal axis of the SHS to the outer shell, and I_{xx} is the second moment of area of the SHS. Once $\overline{\sigma}$ is known, then we compute $\Delta\overline{\sigma}$ from the time series of $\overline{\sigma}$. Lastly, we use Eq. (9) to compute D_i for the ith sea state.

3. Wave-foil interaction model

This section describes the model used to estimate the forces acting on the hydrofoils of the cyclorotor. Each hydrofoil is modelled as a point vortex beneath the free surface. The model has been previously developed and applied to wave cycloidal rotors in the works of Ermakov and Ringwood [43,44] under regular waves and has been validated for attached flow conditions by Arredondo-Galeana et al. [29]. Here, we provide a summary of the model and implement an additional module to consider irregular waves.

3.1. Point-vortex model

The complex potential of a point vortex, under a free surface, was derived by Wehausen and Laitone [45]. This representation has been used widely in wave cyclorotor modelling by Hermans [46], Siegel et al. [47] and Ermakov and Ringwood [43,48] to compute the free surface elevation downstream of the rotor and, recently, to estimate the loads in the hydrofoils of a cyclorotor under attached flow conditions [29,34,44]. In this paper, we utilise this potential flow model to compute the forces on the hydrofoils. We then implement different control strategies and assess the mechanical power and fatigue damage performance.

The point vortex model has been derived in the form of the complex potential in [49] as

$$F(z,t) = \frac{\Gamma(t)}{2\pi\mathbb{i}}\mathrm{Log}\left[\frac{z-\zeta}{z-\zeta'}\right] - \frac{2\mathbb{i}\sqrt{g}}{\pi}\int_0^t \frac{\Gamma(\tau)}{\sqrt{\mathbb{i}(z-\zeta')}} D_w\left[\frac{\sqrt{g}(t-\tau)}{2\sqrt{\mathbb{i}(z-\zeta')}}\right] d\tau, \tag{13}$$

where z is the complex variable, t is time, ζ is the position of the point-vortex, ζ' is the complex conjugate of ζ, Γ is the circulation of the point vortex, g is the gravitational constant, k is the wave number and $D_w[x]$ is the Dawson function denoted by:

$$D_w[x] = e^{-x^2}\int_0^x e^{y^2} dy. \tag{14}$$

The first term of Eq. (13) represents the complex potential of a point vortex of circulation Γ under a free surface. The point vortex is located at ζ. A mirror vortex is located above the free surface at ζ' to impose the impermeability condition. The second term in Eq. (13) represents the complex potential of the waves radiated due to the wake of the foil. We note that the second term typically consists of two integrals, one over time t and another one over the wave number k [46,47]. Here, we use the expression derived in Ermakov and Ringwood [49] which solves the integral over k analytically with the Dawson function. In the integration of Eq. (13), the lifetime of the generated wake is considered to be two full rotational periods of the foil.

The circulation of the point vortices, Γ_1 and Γ_2, is computed from the lift force definition given by Eq. (1), and by applying the Kutta condition, we get

$$\Gamma = F_L/(\rho|U|) = \frac{1}{2} C_L(\alpha)\,|U|\,C. \tag{15}$$

Considering that hydrofoil 1 is located at z, we can evaluate the influence of hydrofoil 2 and the wakes of both hydrofoils on the velocity field at point z. Then, the velocity field $\mathbf{w}_\Gamma$ at point z is obtained as

$$\mathbf{w}_\Gamma = \frac{\partial(F_1(z,t)+F_2(z,t))}{\partial z} = w_{\Gamma x} - \mathbb{i} w_{\Gamma y}. \tag{16}$$

In Eq. (16), the influence of $\partial F_i(z,t)/\partial z$ on foil i is only due to the second term of Eq. (13). This is because when $\zeta = z$, the first therm of Eq. (13) has a singularity. However, the further away the wake vortex is from the foil, the less influence it exerts on the velocity field of the foil, as specified by Dawson's function in Eq. (13). The exact terms for the complex velocity of a two foil cyclorotor, which are used in this work, are those found in Ermakov and Ringwood [49].

Once the velocity field due to the circulation of the foils and their wakes is assessed, we determine the velocity components on the foils due to the rotation of the foils and due to the irregular waves. Then, these velocity components are combined to determine the relative inflow velocity on the hydrofoil, as well as the angle of attack. Then, we introduce the methodology to compute the hydrofoil velocity and the irregular wave velocity components.

3.2. Hydrofoil velocity

The foil velocity components are obtained as follows. Consider a rotor of radius R, as depicted in Fig. 2. The position of the hydrofoils, in cartesian coordinates, is given by

$$x = R\cos(\theta(t) + \psi) \tag{17}$$

and

$$y = y_0 - R\sin(\theta(t) + \psi), \tag{18}$$

where y_0 is the submergence of the rotor, $\theta(t)$ is the angular position with respect to the positive horizontal axis and positive clockwise, and ψ is the initial angular position of each hydrofoil, also measured from the positive horizontal axis. For the rotor shown in Fig. 2, $\psi = 180°$ for hydrofoil 1 and $\psi = 0°$ for hydrofoil 2. The rotational velocity components $\mathbf{u} = (u_x, u_y)$ of the hydrofoils are obtained through derivation of Eqs. (17) and (18), such that

$$u_x = -\dot{\theta}(t)R\sin(\theta(t) + \psi) \tag{19}$$

and

$$u_y = -\dot{\theta}(t)R\cos(\theta(t) + \psi), \tag{20}$$

where $\dot{\theta}(t)$ is the rotational velocity of the rotor.

3.3. Irregular wave velocity components

A JONSWAP wave spectrum is discretised in frequency and used to generate individual waves of wave amplitude A_j, where j, in this case, is the index denoting the individual wave. The procedure to discretise the spectrum is typically used in design studies of different types of WECs [50–52]. We summarise the procedure as follows. The amplitude of the discrete wave components is given by

$$A_j = \sqrt{2S_A(\omega_j)\Delta\omega}, \tag{21}$$

where $S_A(\omega_j)$ is the amplitude of the spectrum at the jth frequency ω_j, and $\Delta\omega$ is the discretisation step of the spectrum.

We utilise the definition of the JONSWAP spectrum provided by the DNV Environmental Conditions And Environmental Loads Practice Manual [53], which states that the JONSWAP spectrum is given by

$$S_A(\omega_j) = A_\gamma\, S_{PM}(\omega_j)\,\gamma^{\exp\left[-0.5\left(\frac{\omega_j-\omega_p}{\sigma\omega_p}\right)^2\right]}, \tag{22}$$

where S_{PM} is the Pierson–Moskowitz spectrum that is defined as

$$S_{PM}(\omega_j) = \frac{5}{16}H_s^2\omega_p^4\omega_j^{-5}\exp\left[\frac{-5}{4}\left(\frac{\omega_j}{\omega_p}\right)^{-4}\right] \tag{23}$$

and

$$A_\gamma = 1 - 0.287\ln(\gamma). \tag{24}$$

In Eq. (22), $\omega_p = 2\pi/T_p$, and $\sigma = 0.07$ if $\omega_j \leq \omega_p$, or $\sigma = 0.09$ if $\omega_j > \omega_p$. Finally, $\gamma = 3.3$ is the spectrum width factor.

The velocity field corresponding to each individual jth wave is computed with linear deep water wave theory [54], such that

$$w_{x,j} = \frac{\pi A_j}{T}e^{k_j y}\cos(k_j x - \omega_j t + \eta_j) \tag{25}$$

and

$$w_{y,j} = \frac{\pi A_j}{T}e^{k_j y}\sin(k_j x - \omega_j t + \eta_j), \tag{26}$$

where A_j, k_j, ω_j and η_j are the height, number, angular frequency, and phase of the jth wave, respectively, x and y are the horizontal and vertical positions of the hydrofoils, as defined by Eqs. (17) and (18), respectively. Each k_j is computed with three iterations of the dispersion relationship [55], where the first iteration assumes $k_j = 1$. The phase of each discrete wave η_j is randomly assigned within a range of 0 to 2π radians.

The total wave induced fluid velocity components $\mathbf{w} = (w_x, w_y)$ are obtained by adding all $\omega_{x,j}$ and $\omega_{y,j}$, such that

$$w_x = \sum_{j=1}^{n} w_{x,j} \quad \text{and} \quad w_y = \sum_{j=1}^{n} w_{y,j}. \tag{27}$$

Lastly, as described in the literature [56], the power J_w available in an irregular wave is defined as

$$J_w = \frac{1}{64\pi}\rho g^2 H_s^2 \lambda T_p. \tag{28}$$

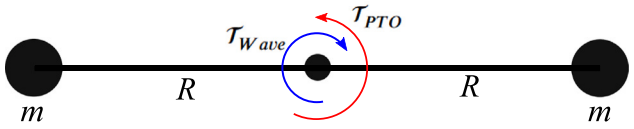

Fig. 11. Two mass system representing the dynamics of the central shaft, where m is the mass of the hydrofoil, R is the radius, $\mathcal{T}_{Wave}$ is the hydrodynamic input torque and $\mathcal{T}_{PTO}$ is the control torque.

3.4. Relative velocity and angle of attack on hydrofoil

The relative velocity **U** acting on the hydrofoil is determined such that

$$\mathbf{U} = \mathbf{w} - \mathbf{u} + \mathbf{w}_{\mathbf{\Gamma_1}} + \mathbf{w}_{\mathbf{\Gamma_2}}, \tag{29}$$

where **w** is the wave induced fluid velocity, **u** is the rotational velocity of the foil and $\mathbf{w}_{\mathbf{\Gamma_1}}$ and $\mathbf{w}_{\mathbf{\Gamma_2}}$ are the induced velocities due to the waves radiated by the foils. Then, we can compute α as the angle between **U** and **u**, as defined in Fig. 2 and by incorporating the effect of ϕ, as illustrated in Fig. 6 for the case of a foil that passively pitches, such that

$$\alpha = \beta - \phi, \tag{30}$$

where,

$$\beta = \sin^{-1}\left(\frac{|\mathbf{U}\times\mathbf{u}|}{|\mathbf{U}|\,|\mathbf{u}|}\right), \tag{31}$$

in agreement with Eq. (8). Once α is computed, a NACA 0015 look-up table is utilised to obtain C_L and C_D for each hydrofoil. Finally, by defining the chord length C and the span of the foil S, and utilising Eqs. (1) and (2), F_L and F_D can be determined. The tangential force in the hydrofoils is defined as

$$F_T = F_L\,\sin(\alpha+\phi) - F_D\,\cos(\alpha+\phi) \tag{32}$$

and the radial force is

$$F_R = F_L\,\cos(\alpha+\phi) + F_D\,\sin(\alpha+\phi). \tag{33}$$

It is worth mentioning that F_T is tangential and F_R is normal to the circumferential path of rotation of the cyclorotor. Therefore, Eqs. (32) and (33) include the term ϕ.

In Eqs. (32) and (33), F_T is responsible for the mechanical power generation, whilst F_R causes the structural load and fatigue of the foil structure.

4. Control strategy

The model for model-based control design of the wave cycloidal rotor is based on Newton's second law for rotation. The rotor rotation in waves is controlled by the power take off (PTO) torque $\mathcal{T}_{PTO}$, allowing the associated electrical machine to function as both a motor and a generator, with the rotor dynamics are determined by

$$I\ddot{\theta} = \mathcal{T}_{Wave} - \mathcal{T}_{PTO}, \tag{34}$$

where I is the inertia of the rotor, $\ddot{\theta}$ is the angular acceleration of the rotor, $\mathcal{T}_{Wave}$ is the hydrodynamic torque and $\mathcal{T}_{PTO}$ is the control torque of PTO. In Eq. (34), the hydrodynamic torque $\mathcal{T}_{Wave}$ is given by

$$\mathcal{T}_{Wave} = (F_{T_1} + F_{T_2})R, \tag{35}$$

where the indices 1 and 2 refer to hydrofoil 1 and 2, respectively. We recall, from Fig. 2, that F_T is the tangential force on the foil and R is the radius of the rotor.

In Eq. (34), the moment of inertia I is estimated as

$$I = 2\,m\,C\,R^2, \tag{36}$$

where m is the mass of one of the hydrofoils. Subsequently, $\mathcal{T}_{PTO}$ can be evaluated from the balance of Eqs. (34)–(36). In Fig. 11, we represent the hydrofoils around the central shaft as a two mass system driven by $\mathcal{T}_{Wave}$ and $\mathcal{T}_{PTO}$, at agreement with Eq. (34). It is worth mentioning that, in this stage of design, the mass of the arms that hold the foils, friction due to bearings, and seals in the rotor assembly are not considered in Eq. (34).

The performance of the cyclorotor is assessed in terms of the average mechanical power generated per second and per span meter, such that

$$J = \frac{1}{T_0\,S}\int_0^{T_0} \mathcal{T}_{PTO}(t)\dot{\theta}(t)dt, \tag{37}$$

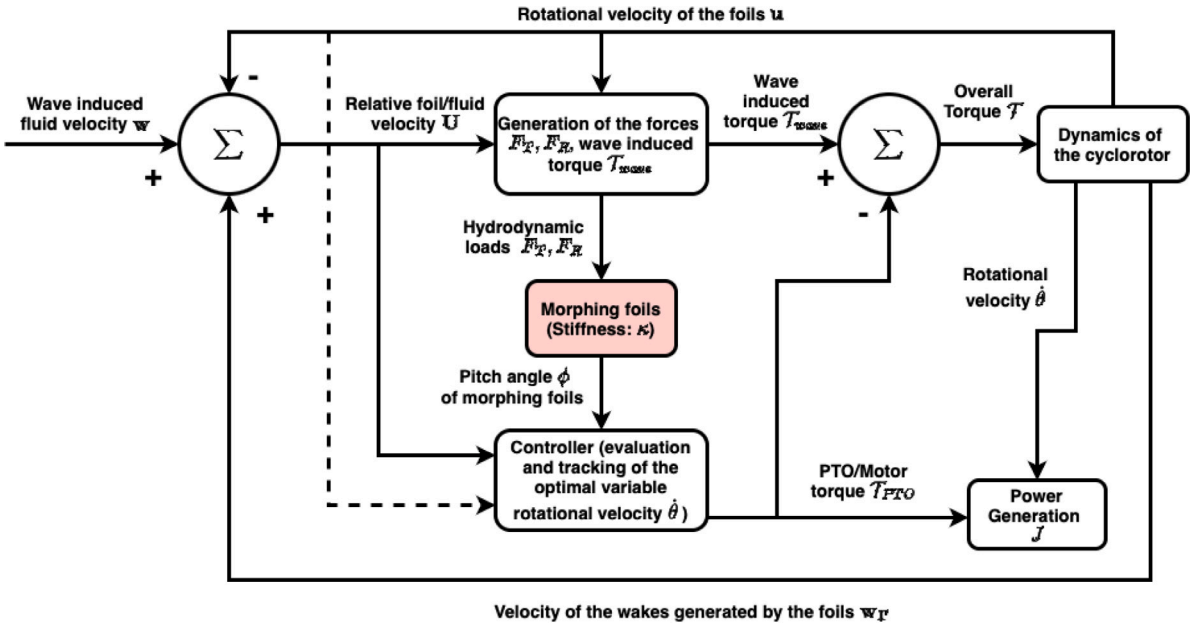

Fig. 12. Control strategy for variable rotational velocity for cyclorotor with passively morphing foils.

where $\mathcal{T}_{PTO}(t)$ is the instantaneous PTO torque, $\dot{\theta}(t)$ is the instantaneous rotational velocity of the rotor, T_0 is the duration of the time interval of the power calculation and S is the span of the hydrofoils. In the following paragraphs, we define the optimal rotational velocity or optimal frequency, at which J is maximised as $\dot{\theta}_0$.

The control objective is to maximise mechanical power generation, which is evaluated in terms of the average mechanical power generated during the time interval $[0, T_0]$, as described in Eq. (37). Thus, the PTO torque $\mathcal{T}_{PTO}$ is calculated to maintain the optimal variable cyclorotor velocity profile $\dot{\theta}(t)$ during the time interval $[0, T]$. The optimal variable rotational velocity $\dot{\theta}(t)$ enables the hydrofoils to achieve an optimal angle of attack α with the wave-induced fluid velocity $\mathbf{w}$, maximising the tangential forces $F_T[\theta, \dot{\theta}]$ on the hydrofoils and, consequently, optimising power generation J. A detailed explanation of the control problem, and relationships between the equations, is presented as a block diagram in Fig. 12. Note that variable rotational velocity control (without morphing foils) has also been implemented and validated during the experimental tests of the 2D and 3D scaled prototypes of the LiftWEC cyclorotor [57–59].

In order to derive the optimal time-varying velocity profile $\dot{\theta}(t)$, a spectral method, which has been proposed in [17,18] and tested in [59], is applied. According to the method, the position of the hydrofoils $\theta(t)$ is presented as a sum of basis functions, in the following form:

$$\theta(t) = \dot{\theta}_0 t + \sum_{i=1}^{h} a_i \cos\left(\frac{2\pi t}{T_{ext}} i + c_i\right) + b_i \sin\left(\frac{2\pi t}{T_{ext}} i + d_i\right), \tag{38}$$

where $\dot{\theta}_0$ is the the reference constant rotational velocity solution at which J is maximised in irregular waves, t is time, a_i and b_i are the Fourier coefficients, c_i and d_i are phase shifts to the harmonic terms of the Fourier series, and h is the total number of harmonics used in the solution.

The corresponding optimal constant rotational velocity $\dot{\theta}_0$, and series coefficients a_i, b_i, c_i and d_i from Eq. (38), can be determined by solving the shaft power J maximisation problem (Eq. (37)). The problem (Eq. (37) and Eq. (38)) should be solved for an extended time period $T_{ext} = 3T_0$, where T_0 is the targeted power production period. Thus, the average power generation J is assessed on the interval $T_0 < t \leq 2T_0$, to eliminate initial and final transients. As part of the optimisation algorithm, the ratio $\dot{\theta}/\dot{\theta}_0$ is constrained to $1/2 < \dot{\theta}/\dot{\theta}_0 < 2$, where $\dot{\theta}$ is the rotational speed specified in Eq. (37), to provide a computationally efficient solution domain. The convergence of the solution within these constraints is shown in [17].

The innovation, which separates the control technique proposed in this article from the method published in [17,18], is that the controller in the current paper includes a control model which is aware of the morphing capabilities of foils. Thus, the morphing foils are now subsumed as part of the model which the control uses to calculate the optimum velocity profile $\dot{\theta}$. An schematic of the control algorithm is provided in Fig. 12.

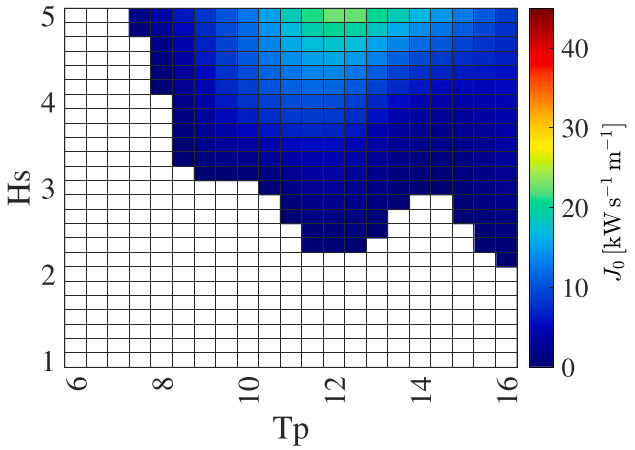

Fig. 13. Average mechanical power J_0 [kW s^{-1} m^{-1}] generated when $\dot{\theta}_0 = \omega_p$, i.e. without optimisation of rotor rotational rate.

5. Results

In this section we present the power performance J and fatigue damage D at the foil stress hot spot, as defined in Eqs. (9) and (37), respectively. We present results for four different control strategies: (1) constant rotational velocity and rigid foil, (2) constant rotational velocity and passively morphing foil, (3) variable rotational velocity and rigid foil, and (4) variable rotational velocity and passively morphing foil. We study J and D over the range of sea states specified in Section 2.3.

Case 1: Constant rotational velocity with rigid foil

The baseline case consists of a wave cycloidal rotor, with rigid foils, spinning at a constant rotational velocity. We consider a cyclorotor with two hydrofoils. The rotor has a radius of $R = 6$ m, the hydrofoils have a NACA0015 cross section with chord length C = 6 m, following the design guidelines proposed by the LiftWEC consortium [3]. We note that these design parameters are also similar to those proposed by the Atargis Energy Corporation [60].

To account for inertial effects, we use a cross sectional mass per square metre of 2 kg/m^2 for each hydrofoil. For the rotor, we consider adjustable submergence that changes with each sea state, such that $y_0 = -1.5R - 0.5H_s$. This promotes efficient power capture by ensuring that the rotor remains in close proximity to the free surface but that the hydrofoils always remain submerged during operation [61].

As a first design step, for each of tested sea states, we match the rotational frequency of the rotor ($\dot{\theta}$) to the peak frequency (ω_p) of a JONSWAP spectrum. We refer to the power under this scenario as J_0, with results as shown in Fig. 13. In the figure, we note that a large portion of the matrix yields $J_0 \leq 0\,\mathrm{kWs^{-1}m^{-1}}$. Although a pitch angle can be introduced to the hydrofoils to increase J_0 [29,60], in this paper, we propose variable velocity control as a mechanism to increase power production. We follow the procedure proposed by Ermakov et al. [17].

The optimal rotational speed is found with the use of high performance computing facilities from the Irish Centre for High-End Computing (ICHEC) (https://www.ichec.ie/) and the ARCHIE-WeST High Performance Computer in Scotland (https://www.archie-west.ac.uk/). For each sea state, we conduct trials of 15 min averaged over 20 different sea state realisations, to ensure statistically significance of the results. The optimal rotational speed is found by varying the rotational speed of the rotor, in steps of 0.1 rad/s, until the maximum power is encountered. We note that this rotational speed maximises the tangential force on the hydrofoils, and therefore, also the lift-to-drag ratio.

Results for the optimal constant rotational speed $\dot{\theta}_0$ are presented in Fig. 14, normalised by ω_p. The figure shows that $\dot{\theta}_0/\omega_p$ grows from low values ($0.2 \leq \dot{\theta}_0/\omega_p \leq 0.5$) to high values ($2.5 \leq \dot{\theta}_0/\omega_p \leq 4.0$) as T_p and H_s increase.

The power output of the rotor running at $\dot{\theta}_0/\omega_p$ is shown in Fig. 15. One realisation per sea state is run for a time period of one hour. Because this is the first control strategy, we denote this power as J_1. Fig. 15 shows that the highest J_1 occurs at the upper right corner of the figure, i.e. J_1 grows with both H_s and T_p. A limited area where $\dot{\theta}_0/\omega_p = 1$ is the only region where the non optimised solution of Fig. 13 and the optimised solution of Fig. 15 overlap. Note that, the shape of Fig. 15 matches the distribution of power available in the irregular waves given by Eq. (28). In fact, assuming a zero pitch angle in the foils, efficiencies of up to 0.15 to 0.20 can be achieved, at the optimal constant rotational speed.

To understand better the damage footprint on the hydrofoil stress hot spot due to P_i, we plot, in Fig. 16a, D_1 assuming $P_i = 1$, while, in Fig. 16b, we plot D_1 considering the P_i shown in Fig. 8. We refer to both results as $D_1(P_i = 1)$ and D_1, respectively. The duration of these runs are the same as those used to compute J_1.

Fig. 16a shows that, the highest $D_1(P_i = 1)$ occurs at the highest H_s and the lowest T_p. This is in contrast to the location of the highest peak in J_1, and therefore contradicts what is typically expected, which is that the location of the peak in damage is usually the same location as the peak in power. However, in the case of the sample stress hot spot analysed in this study, although the peak

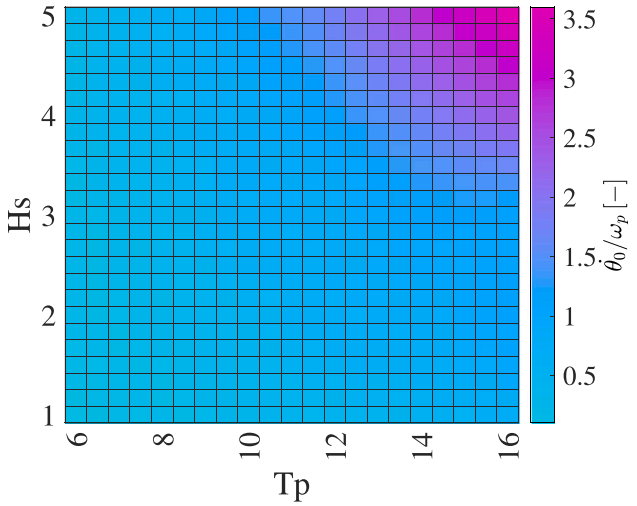

Fig. 14. Optimal normalised constant rotational rate $\dot{\theta}_0/\omega_p$ for various panchromatic sea states.

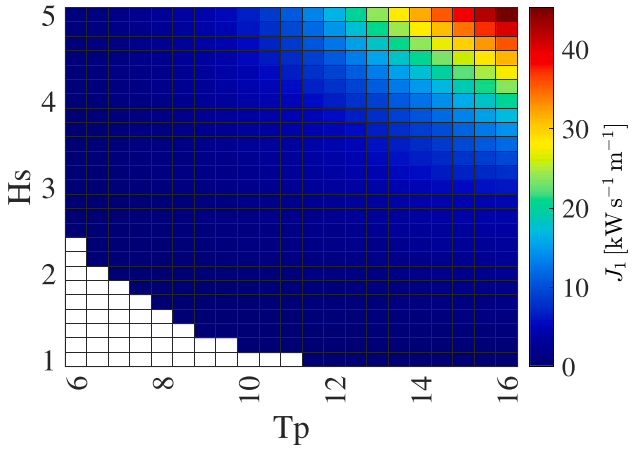

Fig. 15. Average mechanical power J_1 [kW s^{-1} m^{-1}] generated with the rotor operating at $\dot{\theta}_0/\omega_p$.

of both J_1 and $D_1(P_i = 1)$ occur at the highest H_s, the rotor spins faster at low T_p. Hence, more loading cycles occur at the lowest T_p values and therefore more damage occurs, as shown in Fig. 16a.

Then, the effect of P_i in D_1 is shown in Fig. 16b. The location of the highest peak in D_1 is shifted towards intermediate T_p values, but consistently at $H_s = 5$ m. Noticeably, a secondary peak appears at $H_s \approx 3$ m and $T_s \approx 8$ s. The shift in position of the highest peak in D_1 is a result of the distribution of P_i at $H = 5$ m, with the highest P_i at intermediate T_p values. The secondary peak in D_1 is a result of the combined effect of sea states with high probability of occurrence ($P_i \geq 0.14$) and a high number of cycles, due to the fast rotation of the cyclorotor at low T_p. Assuming a span of $S = 10$ m, and offshore steel with cathodic protection, Fig. 16b yields a yearly cumulative fatigue damage of $D_1 = 0.004$. This is equivalent to 25 years of useful lifetime of the hydrofoil, before mechanical failure.

Case 2: Constant rotational velocity with passively morphing foil

Case 2 evaluates the effect of morphing foils, modelled as passively pitching foils, on the performance of wave cycloidal rotors. Similarly to what has been shown in tidal turbines, it is expected that the radial load on the hydrofoil is reduced and consequently, that the bending stresses and fatigue damage are reduced as well. However, because this is the first time that such concept is evaluated in the context of a wave cycloidal rotor, it is unknown to what extent this control strategy can influence the power output.

We recall that the single spring model developed for tidal turbines [28] was developed assuming a nonzero mean angle of attack and periodic oscillations. Hence, such a model is not suitable to represent a morphing hydrofoil in the context of a wave cycloidal rotor, especially and under the influence of irregular waves. Therefore, we compensate the lack of a nonzero mean angle of attack,

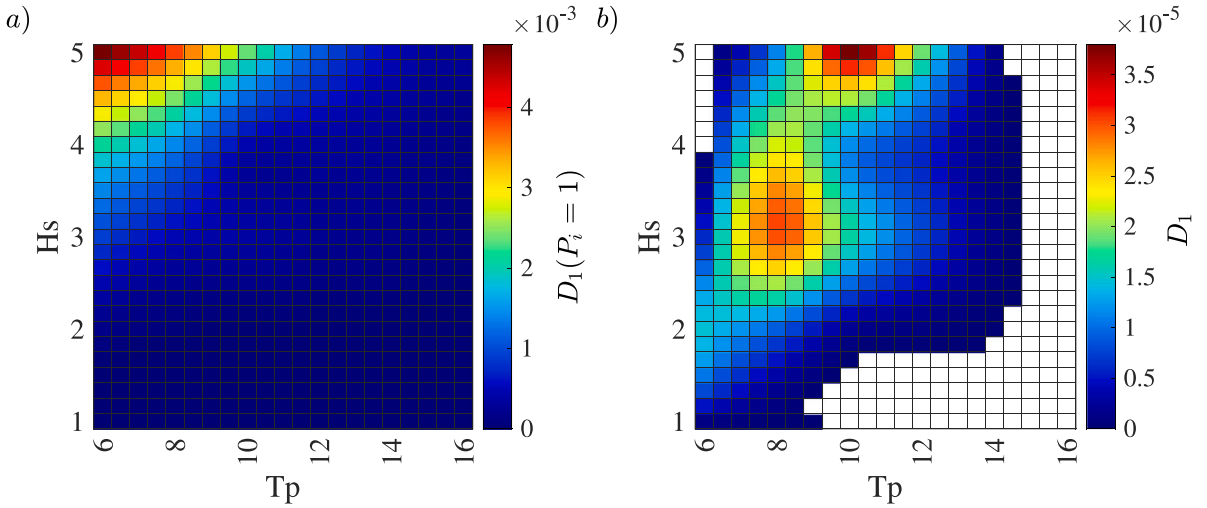

Fig. 16. Yearly damage D_1 at the foil hot spot, generated with $\dot{\theta}_0/\omega_p$ when (a) $P_i = 1$ and (b) when P_i is that of Fig. 8.

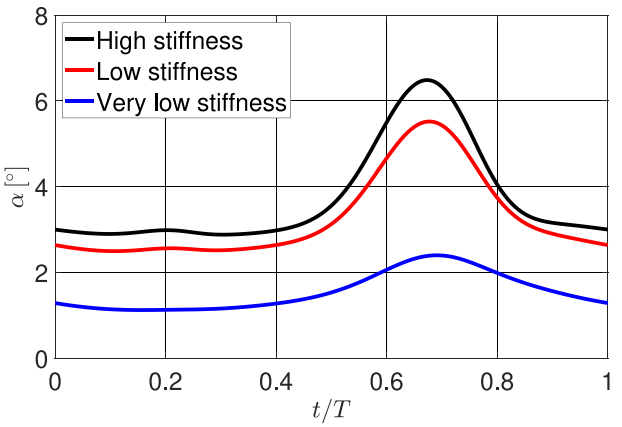

Fig. 17. Changes in angle of attack for one cycle of rotation t/T, computed with κ = 1000, 1 and 0.1 MN/m in black, red, and blue, respectively. Results are presented for hydrofoil 1 and assuming $H = 2$ m and $T = 8$ s in regular sea state test.

and a nonzero mean hydrostatic moment, by incorporating another spring in the model. The second spring allows the hydrofoils of the cyclorotor to sustain the equilibrium position shown in Fig. 5.

We first assess the performance of the dual spring model in a regular wave scenario, where the rotor has a phase shift of −90° with respect to the wave crest [34,43]. In regular waves, the rotor operates typically at a rotational velocity equivalent to the wave frequency $\dot{\theta} = \omega$. We consider a cyclorotor with two hydrofoils, each with a pitch angle of $\phi = 0°$. The rotor has a radius $R = 6$ m and a submergence of $y_0 = -10$ m. For this analysis, we consider a sea state with the highest probability of occurrence shown in Fig. 8, i.e. $T_p = 8$ s and $H_s = 2$ m. The chord length of the foils is C = 6 m.

For the monochromatic sea state test, we evaluate the influence of the spring stiffness κ on the changes of the angle of attack α, within a wave period T. We test three different spring stiffnesses $\kappa = 1000$ MN/m, $\kappa = 1$ MN/m, and $\kappa = 0.1$ MN/m to represent rigid, intermediate and flexible stiffness, respectively. The corresponding changes of the angle of attack in one of the hydrofoils of the cyclorotor are presented in Fig. 17. It can be seen that peak loading alleviation occurs with intermediate and low stiffness. However, the mean angle of attack decreases with lower stiffness. This means that the amplitude of both F_R and F_T will also decrease. Considering these results, a reduction in F_R is desirable in terms of fatigue damage; however, a reduction in F_T is detrimental in terms of power output.

As part of the regular sea state analysis, we also quantify the change in radial loading for the tested hydrofoil (F_R) and the change in power output (J). Assuming a time step of 0.2 s, the high stiffness case $\kappa = 1000$ MN/m, i.e. the rigid foil, yields $J = 13.2$ kW/s, but a peak radial load of $F_R = 48.9$ kN. The medium stiffness case $\kappa = 1$ MN/m, yields less energy, with $J = 11.7$ kW/s, but reduces

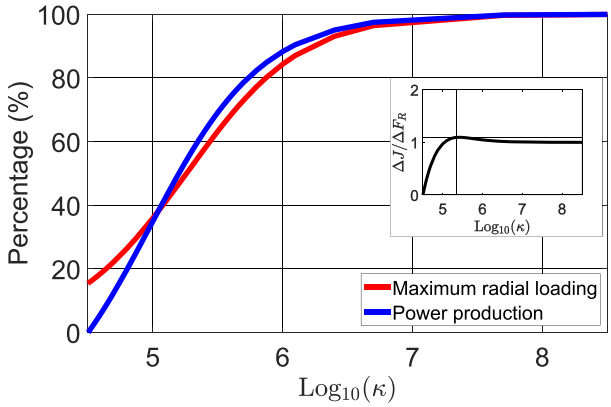

Fig. 18. Power production and maximal radial loading percentage versus spring rigidity. High rigidity ($\kappa \geq \mathrm{Log}_{10}(8)$) yields 100% of power production and maximal radial loading. Results are computed with $H = 2$ m and $T = 8$ s in regular sea state test.

structural loading, with a peak load of $F_R = 41.2\,\mathrm{kN}$. In the low stiffness case, where $\kappa = 0.1\,\mathrm{MN/m}$, both power production and peak radial loading drop significantly to $J = 4.6\,\mathrm{kW/s}$ and $F_R = 1.8\,\mathrm{kN}$, respectively.

The trends in generated power and maximal tangential loads, with different spring rigidities, is presented in Fig. 18. In agreement with Fig. 17, we also consider the sea state with the highest probability of occurrence, i.e. $T_p = 8$ s and $H_s = 2$ m. In Fig. 18, we observe that the lower the stiffness, the lower the power production. This is because, at the starting equilibrium position, the chord line of the hydrofoil is tangential to the circumferential path of the cyclorotor. As such, any pitching motion of the hydrofoil moves the chordline closer to the direction of U. If the spring has very low stiffness, then α on the hydrofoil can be nullified, as illustrated in Fig. 7. Therefore, the stiffness of the spring, and of any material used to manufacture a morphing hydrofoil, should be one that allows load alleviation, but prevents a total loss of generated power.

Once the performance of the passive pitch model was assessed in a regular sea state scenario, we test the model in irregular sea state conditions, for J and D. For Case 2 we refer to these as J_2 and D_2. We utilise simulations of one hour, as we did previously for Case 1. Results are shown for the average power performance J_2/J_1', and the average fatigue damage performance D_2/D_1', in Fig. 19a and Fig. 19b, respectively.

The ratios J_2/J_1' and D_2/D_1', are computed by adding the corresponding J_2, J_1', D_2 and D_1' for each of the simulations performed per sea state, and by calculating their ratio. For Case 2, the number of simulations per sea state is just one, the relatively long simulation of one hour is statistically significant. In contrast, for variable rotational speed, we perform more than one simulation of shorter time length, since they require a higher computational effort. Hence, for the remainder of the paper, the notation J_1' and D_1' are used to highlight that the reference power and damage are recomputed to match the time lengths of the simulations.

For both foils of the cyclorotor in Case 2, we select a spring stiffness of $\kappa = 0.25$ MN/m. This stiffness was selected because for the sea state with the highest probability, it provides about 70% of output power and 60% of radial force loading with respect to the rigid case, as shown in Fig. 18. As such, it is the rigidity that offers the highest power to radial loading reduction ratio ($\Delta J/\Delta F_R$), as shown in the inset of Fig. 18.

Results in Fig. 19a show that $J_2/J_1' \geq 0.90$ for most of the tested sea states, with the exception of the upper right part of the figure, where $J_2/J_1' < 0.8$. However, the probability of occurrence of these sea states is much less than those where $J_2/J_1' \geq 0.90$, therefore, the selected spring stiffness shows satisfactory performance in terms of power production. In fact, the average loss of power of 10% throughout most of the sea states is significantly smaller than the 30% power loss that was computed in the regular sea state scenario.

In contrast, $D_2/D_1' < 1$ throughout most of Fig. 19b. This shows an important reduction in fatigue damage compared to that for a rigid hydrofoil case. In particular, the fatigue damage reduction becomes more significant at high energy sea states where $D_2/D_1' < 0.5$. These results highlight that a hydrofoil that deforms due the fluid loading is useful for wave cycloidal rotors aiming to extend their operational life while incurring a reduced loss in power loss, but also a significant reduction in fatigue damage at the hydrofoil stress hot spot.

Case 3: Variable rotational velocity with rigid foil

We now consider the influence of variable rotational velocity on J and D , initially with rigid foils. For Case 3, we refer to these as J_3 and D_3, respectively. Previous research has shown that variable velocity control can increase the mechanical power by up to 40% [17,18] in monochromatic and also in panchromatic waves. However, the effect of this control strategy, for a wide range of irregular sea states, remains unknown, as well as the impact in the radial loading and the structural penalty at the hydrofoil sample hot spot. Therefore, we investigate these aspects in this section.

It is worth mentioning that the optimisation of the performance function (Eq. (37)) requires the solution of a highly nonlinear problem [43]. In order to achieve acceptable convergence of the developed spectral method (Eq. (38)), it was decided to limit the simulation duration to one minute only. This was achieved with $h = 25$ harmonics in Eq. (38). For Case 3, a total of 5 simulations

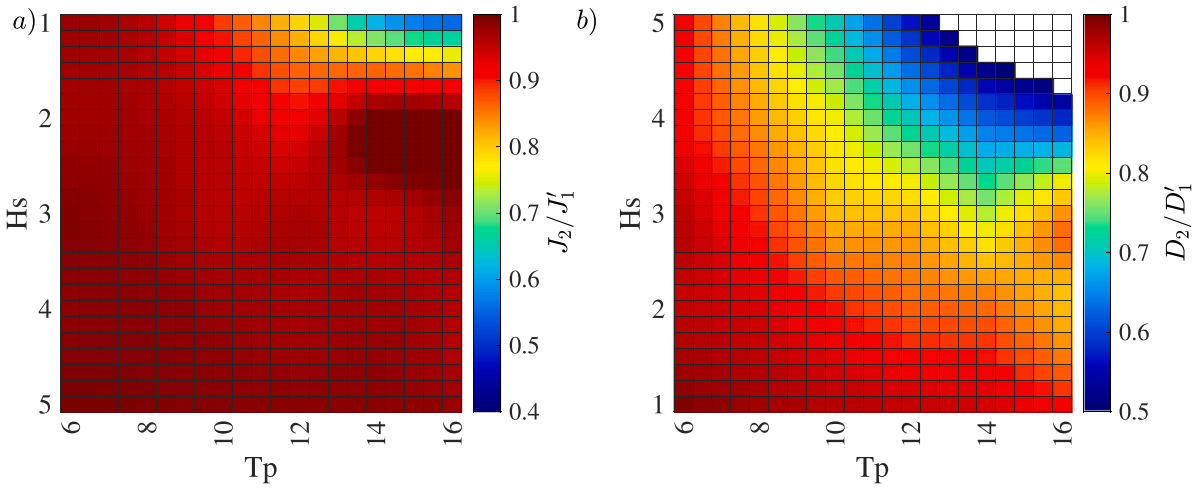

Fig. 19. (a) J_2/J_1' ratio and (b) D_2/D_1' ratio, with passively pitching foils modelled with the dual spring model.

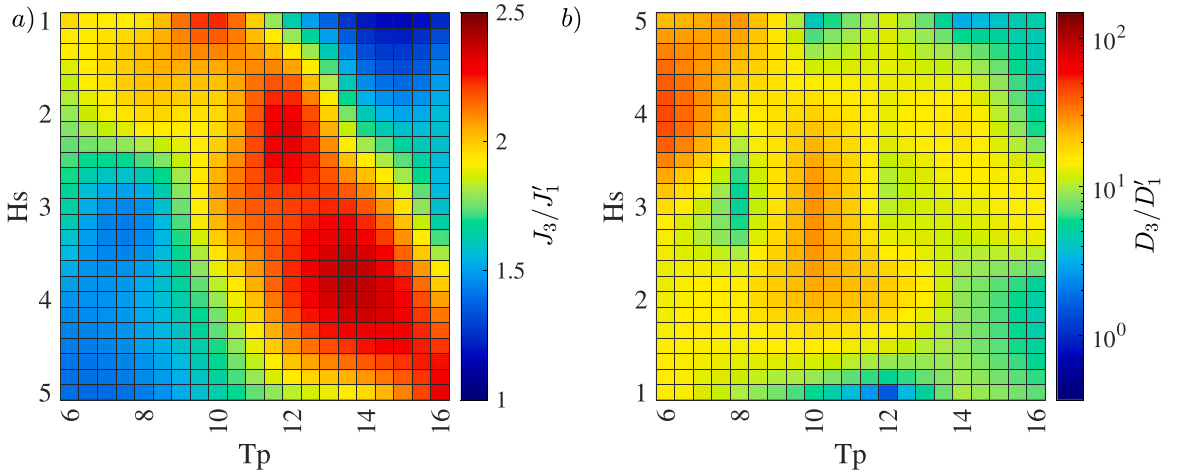

Fig. 20. (a) J_3/J_1' ratio and (b) D_3/D_1' ratio with variable time-dependent rotational velocity.

were performed. The corresponding J_3/J_1' and D_3/D_1' were computed, as described previously in Case 2. The same procedure is applied in Case 4.

Results for Case 3 are presented in Figs. 20a and 20b, respectively. Fig. 20a shows the J_3/J_1' ratio. The figure shows that the ratio remains between $1.5 \leq J_3/J_1' \leq 2.5$. These results represent gains of about 50% to 150% percent with respect to the case of constant rotational velocity. It is noted that Fig. 20a has a similar shape to the power matrix computed with real-time velocity control in monochromatic waves, as presented in Ermakov et al. [17]. This shows that similar power performance can be expected between regular and irregular sea states.

Fig. 20b shows the D_3/D_1' ratio. It can be seen that D_3 is about 10 times higher than D_1'. However, at the top left side of the figure, where low T_p and high H_s occur, D_3 is about 80 times higher than D_1'. This shows that the gain in power comes at the cost of an increase in fatigue damage at the foil hot spot and that, in fact, the increase in damage is significantly higher than the increase in power output. For instance, if we consider that, in general, $D_3/D_1' \approx 10$, variable rotational speed could reduce the lifetime of a 10 m span wave cycloidal rotor from 25 to 2.5 years.

Case 4: Variable rotational velocity with passively morphing foil

In Case 3, we showed that a variable rotational speed and fixed rigid hydrofoils significantly increase J_3/J_1'. However, this gain comes at the cost of a substantial corresponding increase in D_3/D_1'. We recall from Case 2, that passively pitching hydrofoils have the potential to reduce D_2/D_1' at the stress hot spots, although this reduction causes a slight drop in power performance. Here, in Case 4, we combine variable rotational velocity control with passively pitching foils to test whether this combination can yield an increase in J_4/J_1', without a significant penalty in D_4/D_1'.

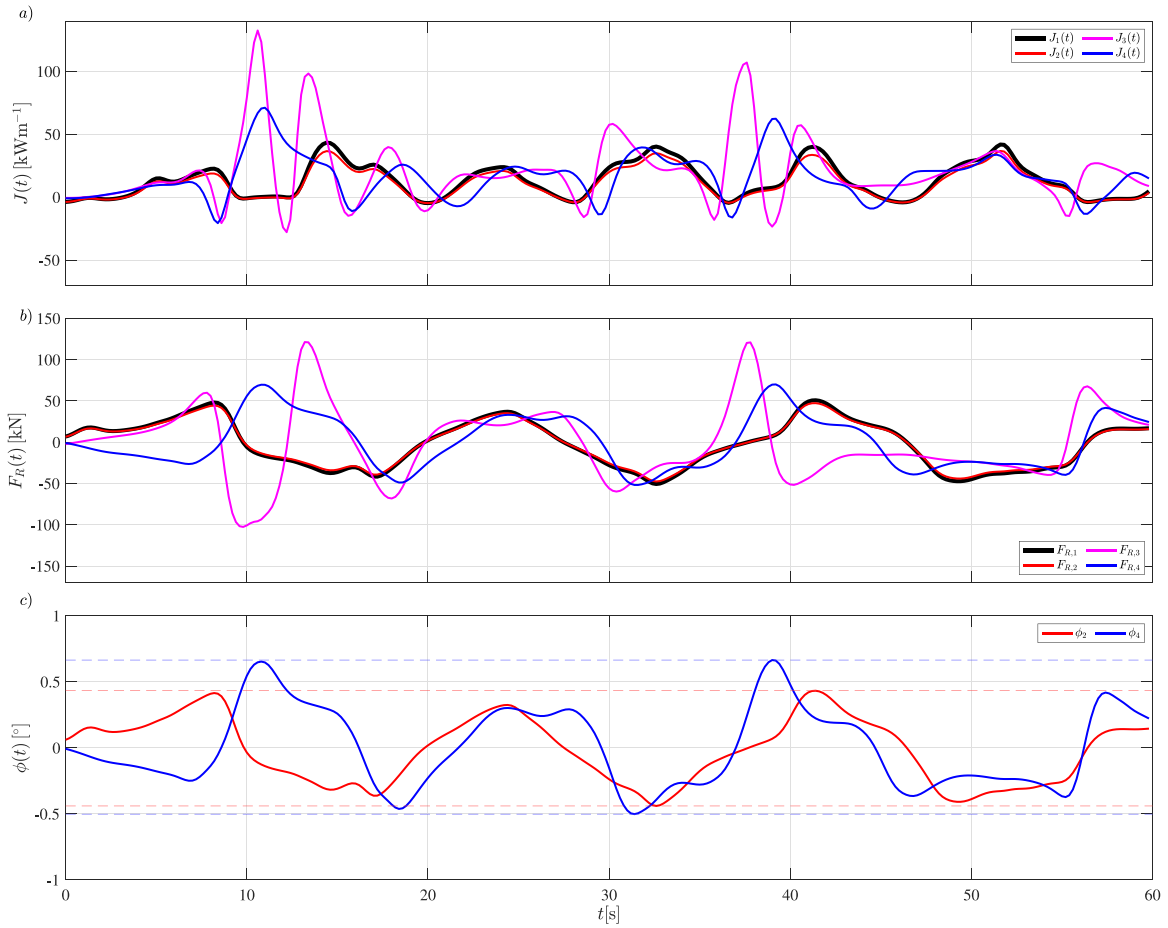

Fig. 21. Results of simulations for Case 1, 2, 3 and 4 during 60 s of high-energy panchromatic wave, with $T_p = 14$ s and $H_s = 4$ m.

Because F_R on the hydrofoils increases due to real-time control of rotational velocity, for this case, we tune the stiffness of the spring in the passively pitching model, by testing the performance of the system in a high energy sea state. As such, we first simulate $J(t)$, $F_R(t)$ and $\phi(t)$ for 60 s of simulation in extreme waves, i.e. $T_p = 14$ s and $H_s = 4$ m.

We compare the results of Case 4 to those of Cases 1, 2 and 3 in Fig. 21. The figure shows the instantaneous J and instantaneous F_R, for the four tested cases in Fig. 21a and Fig. 21b, respectively. We refer to the power production in each case as $J_1(t)$, $J_2(t)$, $J_3(t)$ and $J_4(t)$, and to the radial forces in one of the foils as $F_{R,1}(t)$, $F_{R,2}(t)$, $F_{R,3}(t)$ and $F_{R,4}(t)$. Only the forces for one hydrofoil are presented, since the trends observed in F_R are similar for the second hydrofoil.

In Fig. 21a and Fig. 21b, we plot J and F_R in black, red, magenta and blue solid lines for Cases 1, 2, 3 and 4, respectively. In these figures, J_1 and $F_{R,1}$ are plotted with a thicker line than the other cases, since they represent the baseline case. Then, in Fig. 21c, we show the instantaneous variation of ϕ for the passively pitching cases (Case 2 and Case 4) as ϕ_2 and ϕ_4 in red and blue solid lines, respectively. The dotted lines show the maximum and minimum values of ϕ for ϕ_2 and ϕ_4.

The selected stiffness of the spring used in Fig. 21 is $\kappa = 1.5$ MN/m. This is in the range of low stiffness tested in Fig. 17 and about 6 times higher than the stiffness used for constant rotational velocity and passively pitching foils. This is because, for a cyclorotor with rigid foils, the use of variable velocity increases radial loads and fatigue damage approximately by one order of magnitude with respect to the case of constant rotational velocity, i.e. $D_3/D_1' \approx 10$, as discussed previously in the analysis of Case 3.

Fig. 21a shows that the largest peaks of power occur with variable rotational speed and rigid foils, at J_3, while both of the constant rotational speed cases, J_1 and J_2, show similar behaviour due to the rigidity of the spring. It is observed that variable rotational velocity with passively morphing foils, J_4, corresponds to higher power yield than J_1 and J_2, but a lower yield than J_3. In fact, in Fig. 21a, the average J_1 is 13 kW, while J_2 drops to 11.2 kW. Variable rotational speed increases the average J_3 to 20.5 kW, while the same condition with variable pitching foils, decreases J_4 to 16.6 kW.

This results are in line with the analysis of results previously presented in this Section for Case 1, Case 2 and Case 3. By comparison, Fig. 21b shows that the maximum peaks of F_R also occur in Case 3, i.e. $F_{R,3}$, followed by $F_{R,4}$, $F_{R,1}$ and $F_{R,2}$. In terms of maximum values, $F_{R,3} = 121.0$ kN, while $F_{R,4} = 65.8$ kN, $F_{R,1} = 53.6$ kN and $F_{R,2} = 48.3$ kN. The main difference between Figs. 21a and 21b is that although J is mostly positive throughout the entire simulation, F_R does experience changes in sign and

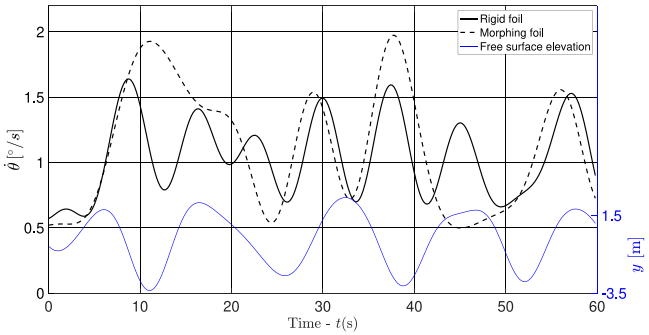

Fig. 22. Free surface elevation above the rotor centre and optimal variable rotational rate $\tilde{\omega}$ control solutions, for the cases of rigid and morphing foils.

can exert compression or tension on the support structure of the hydrofoils. This has an effect on the pitching motion profile of Cases 2 and 4, as show in Fig. 21c. Fig. 21c shows the instantaneous ϕ_2 and ϕ_4, for Cases 2 and 4, i.e. the passively morphing cases. We observe that the trends of ϕ_2 and ϕ_4 follow the trends of $F_{R,2}$ and $F_{R,4}$. This is because the sign of F_R determines the direction of motion of ϕ, as depicted in Figs. 6 and 7. Finally, we recall that the range of motion of ϕ is determined by the stiffness of the torsional spring. We can see that, in Fig. 21c, although both curves are simulated with the same spring stiffness, the range of motion for Case 2 is less severe than the one experienced in Case 4, due to the inclusion of variable rotational speed in the latter.

Importantly, variable rotational velocity and passively morphing foils require a different torque control solution than the case of variable rotational velocity with rigid foils. Therefore the optimal torque solution for each tested sea state needs to be recomputed. As an illustrative example, of how the solution varies between these scenarios, we simulate an irregular sea state of 60 s of extreme panchromatic waves with $T_p = 14$ s and $H_s = 4$ m. The free surface elevation of the simulation is shown, with a blue solid line, in Fig. 22. The variable rotational solutions, for rigid and passively morphing foils, are shown in Fig. 22, with solid and dotted black lines, respectively. By assuming a consistent value of $\kappa = 1.5$ MN/m, we note that both solutions are different to each other, with the passive solution showing smoother transitions between 10 and 25 s, and between 40 and 55 s, with a potential for ease of control as well.

To complete the analysis for Case 4, we plot the J_4/J_1' and D_4/D_1' ratios in Figs. 23a and 23b, respectively. Similar to Case 3, five simulations with a duration of 60 s were run to compute the ratios. Results show that, in general $1 < J_4/J_1' \leq 2.2$. Although these results are slightly lower than those for Case 3, they still show capability of enhanced power production with respect to the baseline J_1'. Furthermore, Fig. 23b shows that D_4/D_1' is further reduced with respect to D_3/D_1'. We recall that Case 3 showed that $10 < D_3/D_1' < 80$, while here, in most of the sea states, $1 < D_4/D_1' < 10$.

Although, $D_4/D_1' > D_2/D_1'$, we recall that the selection of stiffness for the morphing foils used in Case 4 was performed based on a high power sea state ($T_p = 14$ s, $H_s = 4$ m), where $D_4/D_1' < 1$, as observed in Fig. 23b. Furthermore, the spring stiffness was chosen to sustain a high power enhancement ratio throughout most of the tested sea states, as shown in Fig. 23a. Further parametric studies on tuning of the spring stiffness could be carried out individually for each sea state, and the power enhancement ratio could be further reduced to see whether morphing foil technology is applicable to the full range of sea states, or only to high power sea states. It could be, for example, that morphing foils are only usefully deployed in high power sea states, where power production could be further sacrificed for the sake of the structure. However, this is a topic of further research in the field of wave cycloidal rotors.

Transition map between the four tested cases

In this section, we provide a visual map of the four tested cases, as a function of power and fatigue damage at the stress hot spot. The map is shown in Fig. 24 and we utilise the map to show the transition paths between cases. We categorise the cases in red, yellow and green, where green is the most desirable and red the less desirable scenario. In the figure, the horizontal axis denotes power J, while the vertical axis denotes fatigue damage D. The arrows in the figure show how we can transition from case to case by incorporating a single step change in control strategy. From Case 1, we can transit to Case 2 or Case 3, and from Case 2 or Case 3, we can transit to Case 4. The arrows are bidirectional because each control modification is reversible.

Note that, in (red) Case 3, although the gain in J is the highest, it also causes the highest D at the stress hot spots and has the highest potential to damage the hydrofoils of the wave cycloidal rotor. In a (yellow) intermediate category, both Cases 1 and 2 yield a lower D than Case 3, but a lower J as well. Therefore, although these cases are not likely to damage the device, they are likely to capture energy less efficiently. Lastly, Case 4 (green) yields a high J output at a low D. Hence, this is the ideal scenario of operation.

6. Conclusions

In this paper, we present an analytical and numerical study using different control strategies for a two-foil wave cycloidal rotor. Control strategies in a cyclorotor are of particular interest because they have not been extensively explored in the literature and because they could be used to enhance power extraction and mitigate fatigue damage. In this paper, we study the effect of variable

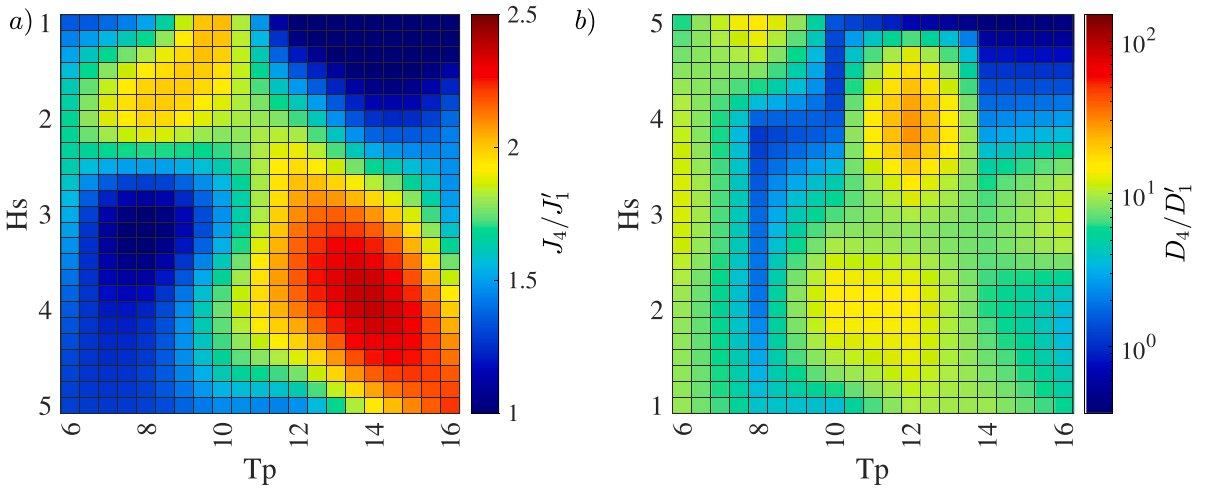

Fig. 23. (a) J_4/J_1 ratio and (b) D_4/D_1 ratio, with variable time dependent rotational velocity and passively pitching foils, modelled with the dual spring model.

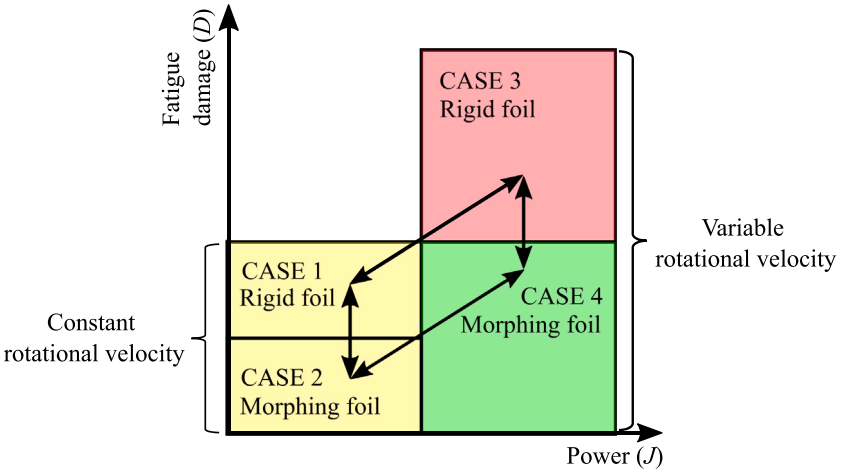

Fig. 24. Transition colour code map between four tested cases showing colour coded severity of cases as green-low, yellow-medium and red-high severity.

rotational velocity combined with, for the first time, passively morphing hydrofoils in irregular waves, in the context of wave cycloidal rotors.

The loads on the hydrofoils are modelled through a single point vortex model, which has been used to estimate wave generation downstream of the rotor and loading on the foils of wave cycloidal rotors [34,44,47,49,60]. We assess rotor performance, using average power output and the fatigue damage at the hydrofoil stress hot spot, as metrics. In this work, we consider a sample stress hot spot located at the fixed end of the hydrofoil, assuming the foil is supported at both ends.

Results are analysed for four different scenarios. Namely, fixed and variable rotational velocity, with rigid and passively morphing foils. Note that, although a variable rotational velocity has previously been shown to enhance power generation in wave cycloidal rotors [17], the structural implications of such control have not been addressed in previous studies. Furthermore, the combined operation of variable rotational velocity with morphing foils has not been performed before in the literature of wave cycloidal rotors.

At constant rotational velocity, the baseline case, we find that there is a specific rotational velocity ω that maximises power extraction for different sea states. This optimal ω usually grows with T_p and H_s. We also show that the fatigue damage distribution is affected by H_s, T_p and P_i. The larger H_s is, the larger the loads on the foils and the fatigue damage. The shorter T_p is, the faster the rotor spins, and therefore, the higher the number of fatigue cycles. Lastly, the distribution of P_i shifts the damage peak towards those sea states with the highest probability of occurrence.

The development of a novel morphing foil model, suitable for a wave cycloidal rotor subject to irregular waves was carried out as part of this study. Our model shows that the passively morphing hydrofoil is effective in mitigating fatigue damage at the sample stress hot spot; however, this reduction in fatigue damage is also associated with a drop in power production.

In order to cope with power losses due to passively morphing foils in the cyclorotor, we explore the concept of variable rotational speed. Our results show that, in agreement with the findings of Ermakov et al. [17,18], there is a time dependent rotational velocity solution that increases power extraction. However, for the first time, we show that variable velocity increases the fatigue penalty in the hydrofoil stress hot spot by a factor of 10 to 80 times, with respect to the baseline case. Therefore, although variable rotational velocity increases power extraction between 50% to 150%, this control strategy, on its own is not sustainable for the long term operation of wave cycloidal rotors. Therefore, we combine variable rotational velocity control with passively morphing hydrofoils to find out, whether an increase in power with a low structural penalty are possible.

The combination of variable rotational speed with morphing foils shows that both a gain in power and a reduction in fatigue damage, are attained. Therefore, we can conclude that variable rotational velocity and passively morphing hydrofoils complement each other to enhance both power production and the structural performance of the cyclorotor. In conclusion, the possibilities for control for wave cycloidal rotors are vast. As such, in this study, we present the first attempt to analyse a few key possible configurations, with the use of high performance computations. Our results show promise to increase both power extraction and at the same time, reduce fatigue damage of the device.

CRediT authorship contribution statement

Abel Arredondo-Galeana: Conceptualization, Formal analysis, Investigation, Methodology, Software, Validation, Writing – original draft, Writing – review & editing. **Andrei Ermakov:** Conceptualization, Formal analysis, Investigation, Methodology, Software, Validation, Writing – original draft, Writing – review & editing, Funding acquisition. **Weichao Shi:** Formal analysis, Funding acquisition, Investigation, Writing – review & editing. **John V. Ringwood:** Conceptualization, Funding acquisition, Project administration, Supervision, Writing – review & editing. **Feargal Brennan:** Conceptualization, Funding acquisition, Project administration, Supervision, Writing – review & editing.

Declaration of competing interest

The authors declare that they have no known competing financial interests or personal relationships that could have appeared to influence the work reported in this paper.

Data availability

Data will be made available on request.

Acknowledgements

This document is the result of the research project funded by the European Union's Horizon 2020 Research and Innovation Programme under Grant Agreement No 851885, and supported in part by a research grant from Science Foundation Ireland and the Sustainable Energy Authority of Ireland under SFI-IRC Pathway Programme 22/PATH-S/10793. Results were obtained using the Irish Centre for High-End Computing (ICHEC) (https://www.ichec.ie/) and the ARCHIE-WeSt High Performance Computer (www.archie-west.ac.uk) based at the University of Strathclyde. The authors would also like to acknowledge the two anonymous reviewers of this work, whose input contributed greatly to improve the quality and organisation of the manuscript.

References

[1] Atargis, the Energy Corporation. 2021, Available: https://atargis.com//. [Accessed: 22 May 2022].
[2] Wu X, Zuo L. Preliminary modeling of angle of attack in self-rectifying turbine under high rotational speed. In: Proceedings of the ASME: the 34th conference on mechanical vibration and sound. 2022, p. 7.
[3] LiftWEC Consortium. 2021, Available: https://liftwec.com/. [Accessed 17 May 2022].
[4] Cao Y, Liu A, Yu X, Liu Z, Tang X, Wang S. Experimental tests and CFD simulations of a horizontal wave flow turbine under the joint waves and currents. Ocean Eng 2021;237:109480. http://dx.doi.org/10.1016/j.oceaneng.2021.109480.
[5] Fernández-Chozas J, Tetu A, Arredondo-Galeana A. Parametric cost model for the initial techno-economic assessment of lift-force based wave energy converters. In: Proceedings of the 14th European Wave and Tidal Energy Conference. 2021.
[6] Bastos P, Devoy-McAuliffe F, Arredondo-Galeana A, Chozas J, Lamont-Kane P, Vinagre PA. Life cycle assessment of a wave energy device – LiftWEC. In: Proceedings of the 15th European Wave and Tidal Energy Conference. 2023.
[7] Cheng Y, Fu L, Dai S, Collu M, Cui L, Yuan Z, et al. Experimental and numerical analysis of a hybrid WEC-breakwater system combining an oscillating water column and an oscillating buoy. Renew Sustain Energy Rev 2022;169:112909. http://dx.doi.org/10.1016/j.rser.2022.112909, URL https://www.sciencedirect.com/science/article/pii/S1364032122007900.
[8] Cummins CP, Scarlett GT, Windt C. Numerical analysis of wave–structure interaction of regular waves with surface-piercing inclined plates. J Ocean Eng Mar Energy 2022;8(1):99–115. http://dx.doi.org/10.1007/s40722-021-00219-6.
[9] Kong F, Su W, Liu H, Collu M, Lin Z, Chen H, et al. Investigation on PTO control of a Combined Axisymmetric Buoy-WEC(CAB-WEC). Ocean Eng 2019;188:106245. http://dx.doi.org/10.1016/j.oceaneng.2019.106245, URL https://www.sciencedirect.com/science/article/pii/S0029801819304238.
[10] Stansby P, Carpintero Moreno E, Stallard T. Large capacity multi-float configurations for the wave energy converter M4 using a time-domain linear diffraction model. Appl Ocean Res 2017;68:53–64. http://dx.doi.org/10.1016/j.apor.2017.07.018, URL https://www.sciencedirect.com/science/article/pii/S0141118717302146.
[11] Zang Z, Zhang Q, Qi Y, Fu X. Hydrodynamic responses and efficiency analyses of a heaving-buoy wave energy converter with PTO damping in regular and irregular waves. Renew Energy 2018;116:527–42.

[12] Ringwood JV, Bacelli G, Fusco F. Energy-maximizing control of wave-energy converters: The development of control system technology to optimize their operation. IEEE Control Syst Mag 2014;34(5):30–55. http://dx.doi.org/10.1109/MCS.2014.2333253.

[13] Ringwood JV. Wave energy control: status and perspectives 2020. IFAC-PapersOnLine 2020;53(2):12271–82.

[14] Bacelli G, Spencer SJ, Patterson DC, Coe RG. Wave tank and bench-top control testing of a wave energy converter. Appl Ocean Res 2019;86:351–66.

[15] Durand M, Babarit A, Pettinotti B, Quillard O, Toularastel J, Clément A. Experimental validation of the performances of the SEAREV wave energy converter with real time latching control. In: Proc. of the 7th euro. wave and todal energy conf. 2007.

[16] García-Violini D, Peña-Sanchez Y, Faedo N, Windt C, Ferri F, Ringwood JV. Experimental implementation and validation of a broadband LTI energy-maximizing control strategy for the Wavestar device. IEEE Trans Control Syst Technol 2021;29(6):2609–21.

[17] Ermakov A, Marie A, Ringwood JV. Optimal control of pitch and rotational velocity for a cyclorotor wave energy device. IEEE Trans Sustain Energy 2022;13(3):1631–40.

[18] Ermakov A, Marie A, Ringwood JV. Some fundamental results for cyclorotor wave energy converters for optimum power capture. IEEE Trans Sustain Energy 2022;13(3):1869–72.

[19] Mohtat A, Fagley C, Chitale KC, Siegel SG. Efficiency analysis of the cycloidal wave energy convertor under real-time dynamic control using a 3D radiation model. Int Mar Energy J 2022;5(1):45–56.

[20] Yang L, Huang J, Congpuong N, Chen S, Mi J, Bacelli G, et al. Control co-design and characterization of a power takeoff for wave energy conversion based on active mechanical motion rectification. IFAC-PapersOnLine 2021;54(20):198–203.

[21] Ermakov A, Ringwood JV. Rotors for wave energy conversion—Practice and possibilities. IET Renew Power Gener 2021;15:3091–108. http://dx.doi.org/10.1049/rpg2.12192.

[22] Whittaker T, Folley M. Nearshore oscillating wave surge converters and the development of oyster. Phil Trans R Soc A 2012;370(1959):345–64.

[23] Arredondo-Galeana A, Brennan F. Floating offshore vertical axis wind turbines: Opportunities, challenges and way forward. Energies 2021;14(23). http://dx.doi.org/10.3390/en14238000, URL https://www.mdpi.com/1996-1073/14/23/8000.

[24] Arredondo-Galeana A, Young AM, Smyth AS, Viola IM. Unsteady load mitigation through a passive trailing-edge flap. J Fluids Struct 2021;106:103352. http://dx.doi.org/10.1016/j.jfluidstructs.2021.103352, URL https://www.sciencedirect.com/science/article/pii/S0889974621001353.

[25] Hoerner S, Abbaszadeh S, Cleynen O, Bonamy C, Maître T, Thévenin D. Passive flow control mechanisms with bioinspired flexible blades in cross-flow tidal turbines. Exp Fluids 2021;62(5):104. http://dx.doi.org/10.1007/s00348-021-03186-8.

[26] Hoerner S, Abbaszadeh S, Maître T, Cleynen O, Thévenin D. Characteristics of the fluid–structure interaction within darrieus water turbines with highly flexible blades. J Fluids Struct 2019;88:13–30. http://dx.doi.org/10.1016/j.jfluidstructs.2019.04.011, URL https://www.sciencedirect.com/science/article/pii/S0889974618309861.

[27] Dai W, Broglia R, Viola IM. Mitigation of rotor thrust fluctuations through passive pitch. J Fluids Struct 2022;112:103599. http://dx.doi.org/10.1016/j.jfluidstructs.2022.103599, URL https://www.sciencedirect.com/science/article/pii/S0889974622000573.

[28] Pisetta G, Le Mestre R, Viola IM. Morphing blades for tidal turbines: A theoretical study. Renew Energy 2022;183:802–19. http://dx.doi.org/10.1016/j.renene.2021.10.085.

[29] Arredondo-Galeana A, Olbert G, Shi W, Brennan F. Near wake hydrodynamics and structural design of a single foil cycloidal rotor in regular waves. Renew Energy 2023;206:1020–35. http://dx.doi.org/10.1016/j.renene.2023.02.068.

[30] Olbert G, Abdel-Maksoud M. High-fidelity modelling of lift-based wave energy converters in a numerical wave tank. Appl Energy 2023;347:121460. http://dx.doi.org/10.1016/j.apenergy.2023.121460, URL https://www.sciencedirect.com/science/article/pii/S0306261923008243.

[31] Lamont-Kane P, Folley M, Frost C, Whittaker T. Preliminary investigations into the hydrodynamic performance of lift-based wave energy converters. In: Proceedings of the 14th European Wave and Tidal energy conference. 2021.

[32] Burton T, N. J, Sharpe. Wind energy handbook. 2nd ed. Wiley; 2011.

[33] Viola IM, Pisetta G, Dai W, Arredondo-Galeana A, Young AM, Smyth AS. Morphing blades: Theory and proof of principles. Int Mar Energy J 2022.

[34] Arredondo-Galeana A, Shi W, Olbert G, Scharf M, Ermakov A, Ringwood J, et al. A methodology for the structural design of liftwec: A wave-bladed cyclorotor. In: Proceedings of the 14th European Wave and Tidal Energy Conference. 2021.

[35] Abbot IH, Doenhoff AE. Theory of wing sections: including a summary of airfoil data. 1st ed. Dover Publications, Inc.; 1959, p. 703.

[36] Veritas D. Recommended practice DNV-RP-C203. Fatigue Design of Offshore Steel Structures. Høvik, Norway: Det Norske Veritas; 2011.

[37] Bai X, Zhao Y, Dong G, Bi C. Probabilistic analysis and fatigue life assessment of floating collar of fish cage due to random wave loads. Appl Ocean Res 2018;81:93–105. http://dx.doi.org/10.1016/j.apor.2018.09.018.

[38] Accensi M, Maisondieu C. HOMERE. Ifremer - Laboratoire Comportement des Structures en Mer. 2015, http://dx.doi.org/10.12770/cf47e08d-1455-4254-955e-d66225c9dc90.

[39] Ahn S. Modeling mean relation between peak period and energy period of ocean surface wave systems. Ocean Eng 2021;228:108937.

[40] Cornett AM. A global wave energy resource assessment. In: Proceedings of the Eighteenth International Offshore and Polar Engineering Conference. 2008.

[41] Mitchell M. Fundamentals of modern fatigue analysis for design. In: Fatigue and fracture. ASM International; 1996, http://dx.doi.org/10.31399/asm.hb.v19.a0002364.

[42] Arredondo-Galeana A, Lamont-Kane P, Shi W, Folley M, Brennan F. A probabilistic framework for fatigue damage of lift based wave energy converters. In: Proceedings of the 15th European Wave and Tidal Energy Conference. 2023.

[43] Ermakov A, Ringwood JV. A control-orientated analytical model for a cyclorotor wave energy device with N hydrofoils. J Ocean Eng Mar Energy 2021;7(2):201–10.

[44] Ermakov A, Ringwood JV. A validated analytical model for a cyclorotor wave energy device. Int Mar Energy J 2022;5(2):201–8.

[45] Wehausen JV, Laitone EV. Surface waves. In: Fluid dynamics / ströMungsmechanik. Berlin, Heidelberg: Springer Berlin Heidelberg; 1960, p. 446–778.

[46] Hermans A, Van Sabben E, Pinkster J. A device to extract energy from water waves. Appl Ocean Res 1990;12(4):175–9. http://dx.doi.org/10.1016/S0141-1187(05)80024-0.

[47] Siegel S, Jeans T, McLaughlin T. Deep ocean wave energy conversion using a cycloidal turbine. Appl Ocean Res 2011;33(2):110–9. http://dx.doi.org/10.1016/j.apor.2011.01.004.

[48] Ermakov AM, Ringwood JV. Erratum to: A control-orientated analytical model for a cyclorotor wave energy device with n hydrofoils. J Ocean Eng Mar Energy 2021;7:493–4.

[49] Ermakov A, Ringwood JV. Development of an analytical model for a cyclorotor wave energy device. In: Proceedings of 14th European Wave and Tidal Energy Conference. 2021.

[50] Jeans T, Fagley C, Siegel S, Seidel J. Irregular deep ocean wave energy attenuation using a cycloidal wave energy converter. Int J Mar Energy 2013;1:16–32. http://dx.doi.org/10.1016/j.ijome.2013.06.001.

[51] Jalón ML, Brennan F. Hydrodynamic efficiency versus structural longevity of a fixed OWC wave energy converter. Ocean Eng 2020;206:107260. http://dx.doi.org/10.1016/j.oceaneng.2020.107260.

[52] Mérigaud A, Ringwood JV. Free-surface time-series generation for wave energy applications. IEEE J Ocean Eng 2018;43:19–35.

[53] Veritas D. Recommended practice DNV-RP-C205. Environmental conditions and environmental loads. Høvik, Norway: Det Norske Veritas; 2007.

[54] Airy GB. Tides and waves, (192). Encyc. Metro.; 1985.

[55] McCormick M. Ocean wave energy conversion. Dover ed. Dover Publications Inc; 2013.

[56] Heller V. 8.04 - Development of wave devices from initial conception to commercial demonstration. In: Comprehensive Renewable Energy. Oxford: Elsevier; 2012, p. 79–110. http://dx.doi.org/10.1016/B978-0-08-087872-0.00804-0.
[57] Ermakov A, Thiebaut F, Payne GS, Ringwood JV. Analytical study of pre-stall hydrofoil experimental data for a cyclorotor-based wave energy converter. In: OCEANS 2023. 2023, p. 1–9.
[58] Ermakov A, Thiebaut F, Payne GS, Ringwood JV. Validation of a control-oriented point vortex model for a cyclorotor-based wave energy device. J Fluids Struct 2023;119:103875.
[59] Ermakov A, Thiebaut F, Ringwood JV. Experimental evaluation of phase and velocity control for a cyclorotor wave energy converter. In: Proceedings of 15th European Wave and Tidal Energy Conference. 2025.
[60] Siegel SG. Numerical benchmarking study of a Cycloidal Wave Energy Converter. Renew Energy 2019;134:390–405. http://dx.doi.org/10.1016/j.renene.2018.11.041.
[61] Ringwood JV, Ermakov A. Energy-maximising control philosophy for a cyclorotor wave energy device. In: 41st International Conference on Ocean, Offshore & Arctic Engineering, no. 80990. American Society of Mechanical Engineers; 2022.

Dr Abel Arredondo-Gaelana is a Postdoctoral Research Associate at the Department of Naval, Marine and Ocean Engineering at the University of Strathclyde.

Dr Andrei Ermakov is a Postdoctoral Researcher at the Centre for Ocean Energy Research, Maynooth University, Ireland.

Dr Weichao Shi was Senior Lecturer at the Department of Naval, Marine and Ocean Engineering at the University of Strathclyde. He is now Reader at the University of Newcastle.

Prof John V. Ringwood is the Director of the Centre for Ocean Energy Research, Maynooth University, Ireland.

Prof Feargal Brennan is Head of the Department of Naval, Marine and Ocean Engineering at the University of Strathclyde.